A Microfabricated Hollow Cantilever Sensor for Sub-nanoliter Thermal Measurements

by

Maxim Shusteff

B.S.E. Electrical Engineering
Princeton University, 2001

SUBMITTED TO THE DEPARTMENT OF ELECTRICAL ENGINEERING
AND COMPUTER SCIENCE IN PARTIAL FULFILLMENT OF
THE REQUIREMENTS FOR THE DEGREE OF

MASTER OF SCIENCE IN ELECTRICAL ENGINEERING AND COMPUTER SCIENCE
AT THE
MASSACHUSETTS INSTITUTE OF TECHNOLOGY

SEPTEMBER 2003

Signature of Author: _____
Department of Electrical Engineering and Computer Science
August 29, 2003

Certified by: _____
Scott R. Manalis
Associate Professor of Media Arts & Sciences and Biological Engineering
Thesis Supervisor

Accepted by: _____
Arthur C. Smith
Chair, Committee on Graduate Students
Department of Electrical Engineering and Computer Science

A Microfabricated Hollow Cantilever Sensor for Sub-nanoliter Thermal Measurements

by

Maxim Shusteff

Submitted to the Department of Electrical Engineering and Computer Science on August 29, 2003 in partial fulfillment of the requirements for the degree of Master of Science in Electrical Engineering and Computer Science

ABSTRACT

A novel design for a cantilever thermal sensor is presented, in which a hollow silicon nitride beam structure encloses a microfluidic channel, through which analytes flow. This scheme is readily integrated with microfluidics for sample delivery, and has a sample volume between 20 and 50 picoliters. Measurements are made by detecting the thermally-induced bending of the cantilever due to its bimorph structure. The cantilevers are fabricated in matching pairs to enable inherently referenced measurements, and interdigitated interferometry is used for sensitive position detection.

Analytical modeling of the mechanical and thermal response of these devices predicts a thermal power density sensitivity of up to 10^{-6} Å /(W/m^3), and a temperature sensitivity of ~300 nm/K at timescales on the order of ~10 ns for most measurement situations. The device resolution for AC-modulated measurements at 50-60 Hz is limited by its thermomechanical noise of approximately 10^{-2} Å /$Hz^{1/2}$.

Prototype devices were successfully fabricated using a sacrificial polysilicon process and used to perform a photothermal spectroscopy measurement with the acridine dye proflavine. The observed absorption peak has a signal-to-noise ratio of about four and correlates well with known absorption data for this dye.

Thesis Supervisor: Scott R. Manalis

Title: Associate Professor of Media Arts & Sciences and Biological Engineering

CONTENTS

LIST OF FIGURES

1 INTRODUCTION

1.1 Thermal Measurements in Biology

The work described in this thesis is concerned with measuring thermal changes and heat flows in biological systems. Such measurements yield valuable insight into the energetics of biological processes. Our overarching research interests lie in making biological measurements simpler, faster, more direct, and using smaller sample quantities, and our goal here is to apply these principles to the thermal energy domain.

1.1.1 Macro-scale thermal methods

One example of a large-scale method is calorimetry: a very general heat measurement technique that can be applied to a great many different chemical or biological systems. Modern calorimetry instruments normally consist of an enclosed vessel, with a typical volume of a few milliliters, into which the sample under investigation is placed. The heat evolved over time within the sample is then quantified using thermoelectric transducers. These instruments can be applied to studying an impressive variety of problems, including molecular kinetics and thermodynamics (e.g. peptide or nucleic acid binding and interaction, conformational changes); heats of dissolution and mixing; sorption processes; stability, curing and degradation; and general thermal process monitoring. Even pieces of living tissue can be placed within a sample vessel [1, 2].

Another useful thermal measurement method is photothermal spectroscopy, valuable for studying optical absorption and energy transitions within a sample. This is a measurement of wavelength-dependent light absorption by a sample, by detecting the heat generated when light is

absorbed. The absorption spectra measured this way are used in analytical chemistry, and biochemical analysis. While this can be a very sensitive technique, it must always be done in a custom-designed apparatus [3], and sample sizes must be at least microliters to milliliters in volume.

Despite being quite well-developed and standardized, these macro-scale thermal methods suffer from several fundamental limitations that limit their applicability. One general problem is poor throughput, as changing samples is awkward and experiment timescales are long. But the most significant shortcoming is the relatively large vessel volume and correspondingly large quantities of sample material (μmoles) that they require. In comparison to molecular and cellular size scales, these requirements are enormous, and high sensitivity in these measurements is only achieved by virtue of averaging over a large number of molecules. This condition makes it impossible to perform ordinary large-scale thermal measurements in many commonly-encountered situations when only a tiny quantity of a particular bio-molecule is available (e.g. having been extracted from a cell culture). It is clear, therefore, that extending thermal methods to allow sensitive, fast-throughput, low-volume measurements would be tremendously useful.

1.1.2 Smaller-scale approaches

Thus far, little research has been carried out on thermal measurement systems at scales approaching single-cell volumes. However, two techniques that have been reported suggest promising avenues of research.

The more recent of these is a picoliter-scale "nanocalorimeter" built by Johannessen and co-workers at the University of Glasgow [4]. This device uses a circular sample well (Fig. 1.1), the bottom of which is a thermopile transducer that measures the generated heat. The structure is microfabricated and has a total volume of 270 pL. The authors report a detection limit on the order of 10 nW, and a thermal time constant of 12 ms, for sample volumes as small as 60 pL. The samples to be measured are microinjected onto the sensor surface, and "capped" with liquid paraffin to prevent evaporation.

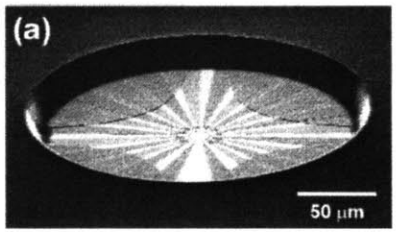

Figure 1.1: Nanocalorimeter sample well. The floor of the well is a series of Ni-Au junctions, making up a thermopile. The wall material is polyimide; its 23μm thickness defines the well depth. (Reprinted from [4].)

The other approach uses the bending of a microfabricated cantilevered beam for heat sensing. This device has been used to perform scanning calorimetry to measure phase transition

energy in nanogram samples of *n*-alkanes (paraffins) attached to the cantilever tip [5], and to measure photothermal absorption spectra of molecules deposited on the cantilever surface [6]. The sensor's thermal time constant is sub-ms, and the authors report a 150 fJ detection limit.

Both schemes are promising steps toward nanoliter-volume heat measurement. Both have problems, however, from the standpoint of capturing the thermal energy evolved in the measured samples. Furthermore, bringing samples to the sensor is extremely cumbersome in both cases, and potential methods to integrate sample delivery systems have not been explored. It becomes apparent that in order to create a small-scale thermal sensor useful for biological measurements careful attention must be given to heat transfer between sample and sensor, as well as to facilitating sample throughput and transport to the sensor.

1.2 Cantilever Sensors

Sensors based on microfabricated cantilevered beam structures have been in use for several decades. Often referred to simply as "cantilevers," their most well-developed application today is for use as probes in scanning probe microscopy (SPM). With the advancement of micromachining technologies, researchers have worked to develop a number of other uses for these flexible, slender, free-standing structures. Much of this work has been aimed at improving and extending the capabilities of SPM, including operating many probes in parallel [7], implementing different detection schemes (piezoresistive, interferometric) [7, 8], and realizing direct maskless lithography techniques [9, 10]. Besides this, cantilever sensors have also been used for strain and vibration measurement, and as acoustical transducers, flow sensors and even valves.

Much recent interest has been focused on using cantilever sensors for molecular detection and other applications in the bio-sensing domain. Cantilevers have been used to observe chemical reactions in real time [11], and as ambient chemical detectors [12, 13, 14]. As we have already seen, some researchers have used cantilevers as thermal sensors [5, 6, 15]. Others have used them to detect molecular binding events resulting from changes in surface stress [16, 17]. Still others have integrated electronic detectors onto cantilevers for molecular probing [18], and resonating cantilevers have been used for mass detection of adsorbed molecules [19]. Clearly taking advantage of the properties of these structures yields many novel and useful applications where nanotechnology meets biology.

In general, as we have seen, scaling down the size scale of biological measurements is a desirable goal. We therefore investigate the potential of our cantilever sensor for carrying out nanoliter-scale thermal measurements on biological samples. The high sensitivity, small volume, and well-controlled heat transfer properties of a cantilever make it attractive for this application. While the device described herein is perhaps not the ultimate biological thermal sensor, it is hoped that sensor scaling and integration can help direct biological research towards high speed and throughput assays, which can be done in parallel on many nanoscale samples.

1.3 Device Concept

This thesis describes a cantilever sensor innovation aimed at biological applications, which introduces an entirely new way for the sensor to interact with the measured sample. For making measurements on biological systems, a liquid environment is very much preferable, if not required, and fluidic connections are often needed to achieve this. Rather than immersing the cantilever in a fluid sample, or delivering the sample to its external surface, we make the cantilever hollow, flowing the sample through a U-shaped fluid channel on the inside (Figure 1.2).

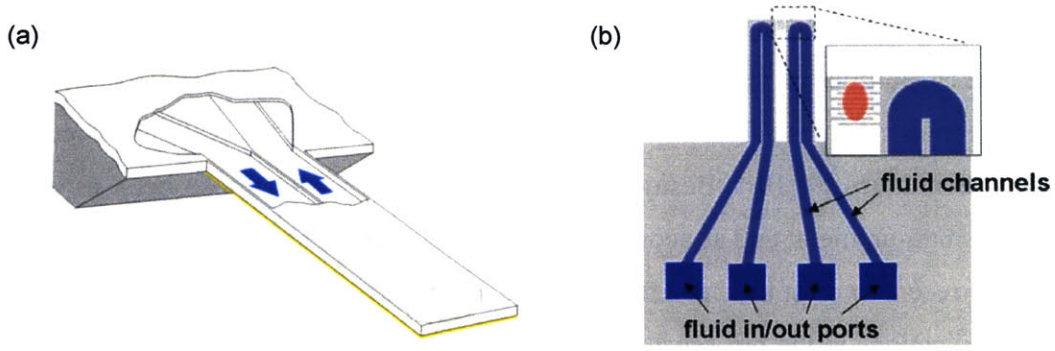

Figure 1.2: The microchannel cantilever. (a) Cut-away conceptual drawing, showing a single cantilever with its internal fluid channel, which is continuous with channels on the supporting die. (b) Top view showing a pair of devices with their fluid channels and access ports; inset shows interdigitated fingers and laser spot, for position detection (see Sec. 2.1.2).

This channel is continuous with other fluidic channels on the supporting silicon substrate. Since the cantilever beam is, effectively, a free-standing microchannel itself, integrating it with a microfluidic network for sample delivery is natural and highly effective. With this scheme, we not only maintain the liquid environment needed for biological assays, but our measured sample's

volume is precisely controlled by the dimensions of the device, and is held entirely within the sensor. This total volume is between 20 and 50 pL, which is equivalent to the volume of only a few eukaryotic cells. We describe the benefits of this design throughout the thesis, along with the special challenges that it presents.

1.4 Thesis Overview

Chapter 2 describes the detailed features of the device design, including key enabling ideas, as well as the main parameters of the prototypical hollow cantilever sensor. Some variations on the basic design, which may prove useful in certain situations, are introduced. We also describe the packaging that is needed for a complete experimental system with these devices. Finally, we touch briefly upon the fabrication techniques used to make the cantilevers.

In Chapter 3, analytical models are used to predict the thermal and mechanical behavior of the hollow cantilever in response to applied loads. We derive the temperature and heat power sensitivity of the structure, and combine those results with device noise estimates to determine the types of measurements that are possible with it. We also examine the effects on cantilever performance of the design variations introduced in Chapter 2.

Chapter 4 describes the setup and details of a photothermal spectroscopy experiment, in which this sensor was used. We show some preliminary results that demonstrate the functionality of the device.

Finally, Chapter 5 deals with future work that will improve the operation of this measurement system, as well as additional experiments and measurements that will be carried out with it.

2 DESIGN

2.1 Enabling Concepts

Three major enabling concepts are fundamental to the device's operation: the thermal bimorph, interferometric position detection, and differential measurement.

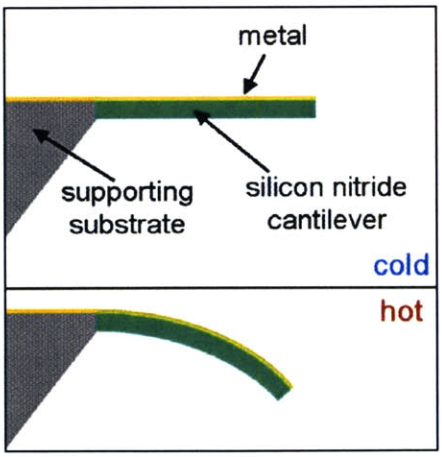

Figure 2.1: Thermal bimorph concept. A temperature rise causes thermal expansion in the cantilever materials. Since the metal expands more than the nitride, the entire cantilever bends (vertical dimensions are greatly exaggerated).

2.1.1 Thermal bimorph

This is the means by which thermal energy changes in the device are transduced into mechanical strain and, consequently, beam deflection, which enables measurement of the heat flow in the device. In a thermal bimorph, two different materials with unequal thermal expansion coefficients are sandwiched together, such that any temperature changes cause unequal thermal strain in the two layers, making the entire structure bend (Fig. 2.1). For the hollow cantilever, the structural material is silicon nitride (SiN_x), and the bimorph structure is realized by evaporating a thin layer of metal on one side of it – typically aluminum. This also provides an excellent reflective surface for interferometry, described in the next section. Measuring the deflection of the

beam gives a measure of the heat flow or the temperature change that caused it. The analytical model used to relate beam deflection to heat flow and temperature change is presented in the next chapter.

2.1.2 Interdigitated (ID) interferometry

Of the different methods that can be used to measure the bending of microcantilevers, the most common is the optical lever, as used in the atomic force microscope (AFM). Cantilever bending is observed by measuring the position of a laser spot reflected from the cantilever tip. Another optical method, with some advantages over the optical lever is diffractive interferometry with interdigitated (ID) fingers, used recently in various applications, such as the AFM [8], accelerometers [20], and stress-based microcantilever sensors [21, 19].

The operating principle is based on a diffraction grating, which is formed by two sets of interspersed microfabricated "fingers." When the phase-coherent light of a laser beam is focused on this grating, it reflects as several diffracted beams, referred to as modes, whose intensity modulates as the finger sets displace out of plane relative to one another (see Figure 2.2). By fabricating a set of ID fingers between the tips of the two cantilevers, and measuring the intensity modulation of a single reflected laser mode, the bending of the cantilevers relative to each other can be measured with sub-angstrom precision. Additional sets of fingers between each cantilever and a fixed area of the die can be used to provide absolute deflection information for each cantilever individually.

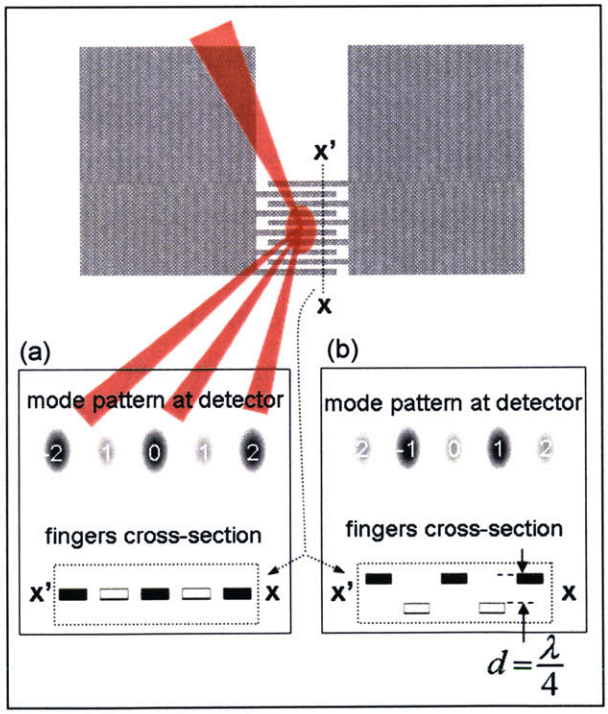

Figure 2.2: ID interferometry. The incident laser beam reflects from the diffraction fingers to produce a pattern of bright and dim modes at the detector (labeled -2 through 2). Their brightness changes as the two sets of ID fingers displace out-of-plane relative to one another –a displacement of $\lambda/4$ is shown between (a) and (b) (see also Section 4.2.2).

The major advantage of using ID interferometry over the optical lever is twofold. First, as described by Yaralioglu *et al.* [22], the measurement is more sensitive than either optical lever or piezoresistor detection. Second,

each measurement is inherently referenced, either to a fixed position, or to a matched cantilever, which is not the case with the optical lever. There is also the minor benefit of lower precision required in detector alignment, since the diffracted modes do not change position; however, this is partially offset by the higher precision required for aligning the measurement laser.

2.1.3 Differential measurement

When making any sort of measurement, performing a reference or control experiment is always required, to eliminate any non-specific effects and isolate the experimental variable (in our case, the thermal characteristics of a particular bio-molecule). Such a control measurement must often be done separately, and subtracted from the experimental data. The ID position detection scheme, however, lends itself very easily to making a measurement that is inherently referenced. The benefit of using such a method has already been reported by Savran *et al.* [16, 21], and we take advantage of it in our design.

As seen in Fig. 1.2 (b), cantilevers are designed in matched sets of two, with identical geometry, and a set of ID fingers between them can be used to measure the differential deflection between two cantilevers, such that one cantilever acts as a built-in reference for the other. This provides real-time rejection of any common-mode signals resulting from nonspecific background disturbances unrelated to the molecule being studied, such as ambient temperature fluctuations, table vibrations, changes in light level, nonspecific adsorption of molecules to channel walls, etc. For instance, using a differential cantilever pair, Savran *et al.* report a 50-fold reduction in sensitivity to ambient temperature fluctuations over that of just a single cantilever [16]. Thus, for example, one of our cantilevers can be filled with the analyte molecules dissolved in aqueous buffer solution, while the other is filled only with the buffer, providing an ideal arrangement to only detect specific signals from the analyte molecules themselves.

2.2 Sensor Design

2.2.1 Key design details

Initial cantilever design decisions were motivated primarily by the aim of achieving high thermal sensitivity in the device, while incorporating the three enabling concepts mentioned above. The basic design therefore includes a pair of hollow cantilevers with a U-shaped fluid

channel passing through each one, and with a set of ID fingers fabricated between the beam tips for relative position detection. As previously mentioned, the thermal bimorph is made by depositing a thin film of metal on one side of the cantilever. Figure 2.3 shows the overall geometry for two different hollow cantilever sensor designs used throughout the course of this work (see Section 2.4).

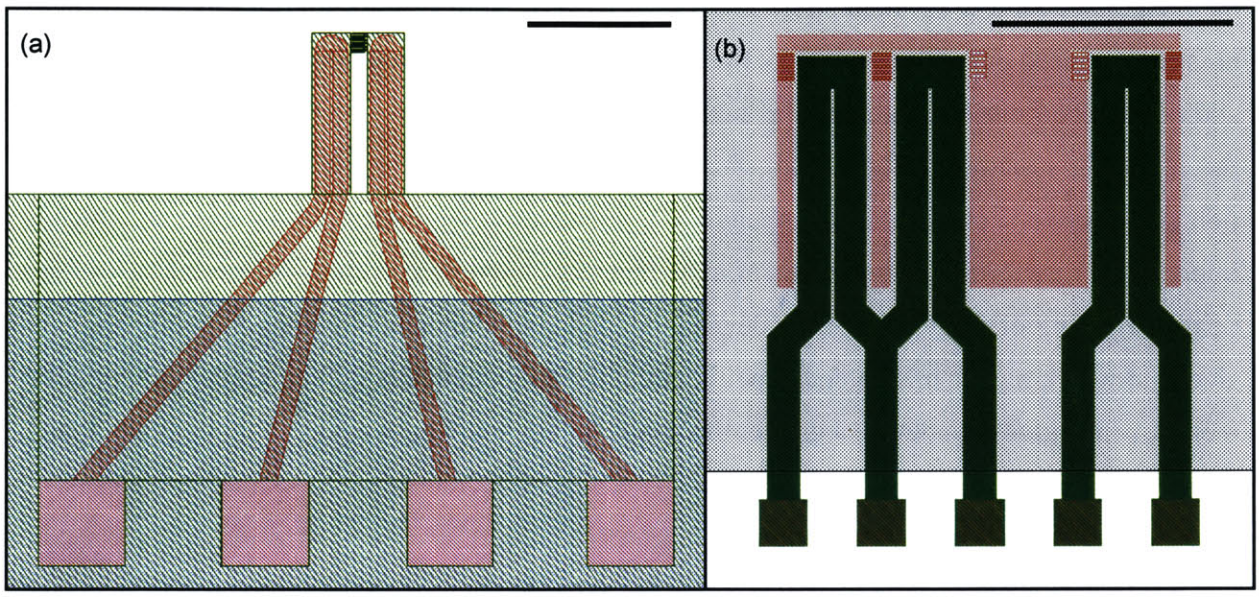

Figure 2.3: Cantilever mask layouts. Two different device layouts as drawn in Cadence, the CAD software used for mask layout. (a) 500 μm long and 100 μm wide cantilevers with separate fluidic channels, used with the bonded wafer process (see Section 2.4) (b) 500 μm long and 160 μm wide cantilevers, which share a common fluid channel, designed for and fabricated using the polysilicon sacrificial process (see also Figure 2.8). The black scale bar in each drawing is 500 μm. For process and mask details, refer to Appendix A.

An approximate device performance target was to achieve temperature sensitivity on par with Savran's differential stress sensor [16], which is a solid nitride cantilever ~1 μm thick, 100 μm wide, and 500 μm long[1]. After some preliminary calculations, and prior to rigorous analytical modeling, a set of "default parameters" was chosen for the hollow cantilever sensor. This was done simply to have a starting point of reference within the parameter space that would give reasonable performance and be realistic to fabricate. These default parameters are defined as follows: beams that are 500 μm long, 100 μm wide, and 1.75 μm thick, (using 500 nm of top and bottom nitride, and a 750 nm thick fluid cavity) with a 100 nm aluminum metal layer. In the next chapter, we will examine in detail the effects that these parameter choices have on the be-

[1] This device has a sensitivity of 3.0×10^{-4} K/Å, or 334 nm/K, with these dimensions: 500 μm long, 100 μm wide, 1 μm thick silicon nitride, and 50 nm thick aluminum metal (compare with hollow cantilever sensitivity, Section 3.3).

havior of the device. Much of this geometry can be varied in the fabrication process, and our aim will be to determine which dimensions should be pushed to the limits of fabrication to obtain the optimal performance from the sensor.

The choice of materials is dictated by a few fabrication and device performance constraints. Low-stress (silicon-rich) silicon nitride (SiN_x) is used as the main cantilever structural material, since its low residual stress allows the fabrication of cantilevered beams with little or no stress-induced curvature – a critical requirement for an interferometric deflection sensor. In addition, silicon nitride also serves as a nearly perfect etch mask for KOH, which is crucial for the cantilever structures to be able to stand up to the long release etch at the end of the fabrication process (see Section 2.4 and Appendix A). Finally, nitride is optically transparent, which is important for performing some types of experiments of interest, as well as permitting in-situ optical monitoring of fluid flow in the device. Aluminum is the metal of choice, being inexpensive, and with a higher-mismatched coefficient of thermal expansion to SiN_x than other common metals, which gives the device a greater thermal response (see Section 3.3).

2.2.2 Major design variations

At design time, several issues prompted consideration of two additional elements that could be added to the basic hollow cantilevered beam structure. The first concern was the fabrication challenge of producing hollow fluidic structures with the extreme height-to-width aspect ratio (1:100) that our design requires. Anticipated problems included channel collapse and stiction, cantilever breakage, and poor fluid flow. A means of stabilizing the channels was therefore introduced: subdividing the fluid channels. Some devices were eventually fabricated with the U-channel subdivided into six small channels, as shown in Figure 2.8(b) below. This scheme does improve fabrication yield, and in Section 3.4 we evaluate the effect of this change on device performance.

The second design alternative aims to increase signal strength. Though the purpose of this device is to do thermal measurements at such small scales, at design time it was uncertain whether the standard tiny fluid volume of ~50 picoliters would produce enough of a response from the hollow sensor. In order to have a greater possible range of total internal volume, a "container" was added onto the end of the cantilever. Figure 2.4 shows a concept drawing of this idea. This is a section with a thickness significantly greater than the thermal bimorph – 10-100

μm – which is not intended to bend, but whose purpose is to serve as a fluid vessel to potentially boost the thermal signal with its greater volume. By selecting the depth and geometry of this vessel, we can precisely vary the sample volume contained within the cantilever through the 10 pL – 1 nL range. At the same time, we retain thermal sensitivity by keeping the inner cantilever section as a thin, flexible bimorph. We examine this option in greater detail as well in Section 3.4.

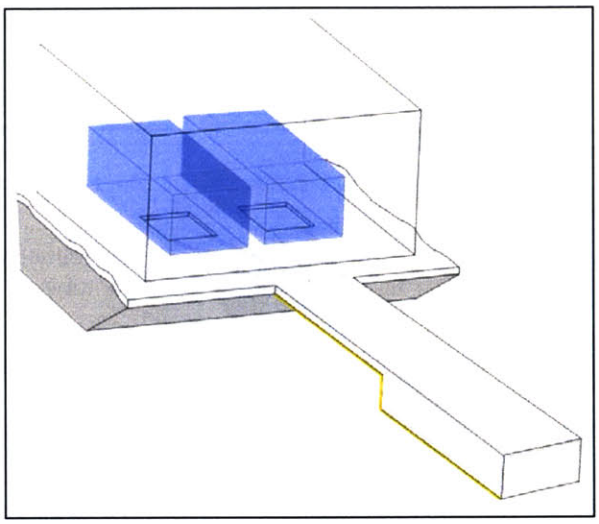

Figure 2.4: Hollow cantilever with a vessel. Conceptual drawing showing a single cantilever and vessel, as well as its associated on-chip elastomer fluidic channels.

2.3 System-Level Design

2.3.1 Packaging

In order to enable experiments with these devices, world-to-chip connections must be made, between some type of macro-scale fluid delivery system and the micro-scale integrated cantilever fluid channels. The simplest and most adaptable scheme for doing this is to use molded poly-dimethylsiloxane (PDMS) elastomer fluid channels bonded to the silicon die. Polyethylene tubing is inserted into access holes punched through the PDMS block, and used to deliver samples to the microfluidic network. PDMS fluidics can be made quickly, and with a short design cycle time, using techniques developed in the Whitesides group at Harvard [23] and further refined over the course of this work. We take advantage of these methods and their simplicity; however, assembling a complete system still proves quite complex and elaborate.

Briefly, PDMS fluidics fabrication begins by creating a master mold on a standard 4" silicon wafer by spin-coating and patterning SU-8 (Microchem Corp.), a negative epoxy-based photoresist. PDMS two-part elastomer (Sylgard 184 from Dow Corning) is mixed, poured onto the silane-treated mold (to prevent adhesion), and cured for 30 minutes at 80° C. After this, the PDMS is peeled off the mold, ready for use, while the mold can be reused many times without any additional processing. After oxygen plasma activation, PDMS blocks with smooth surfaces

can be subsequently bonded to many materials, including glass and silicon nitride, creating leak-tight seals.

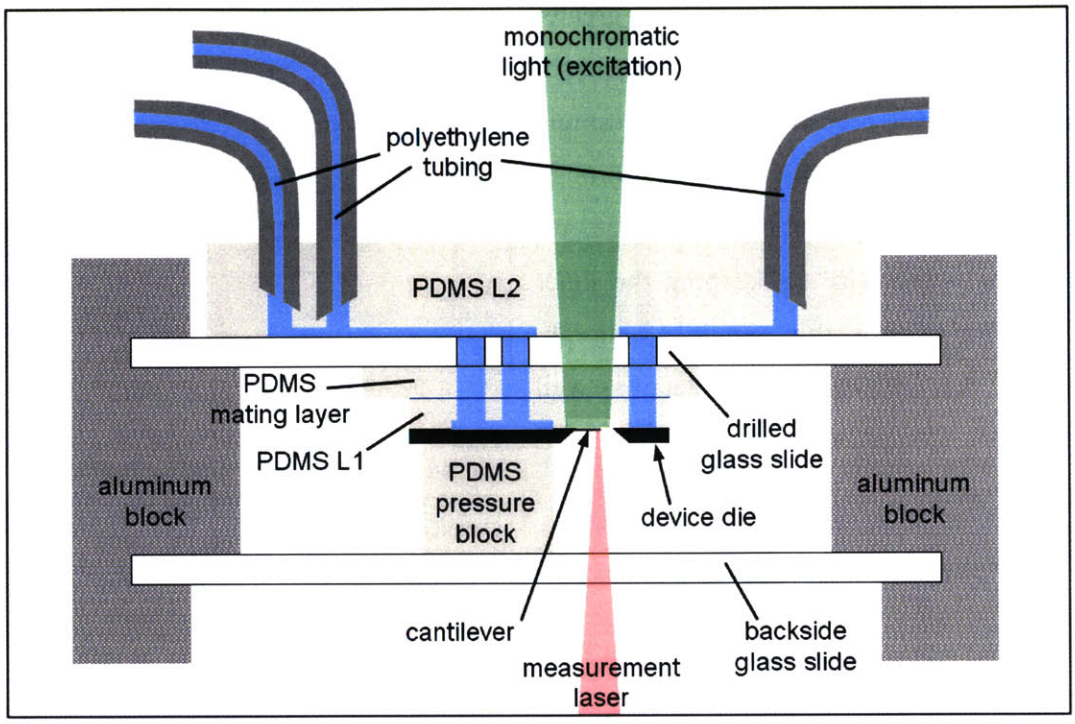

Figure 2.5: Device package schematic. A side-view cross-section through the package chamber, indicating key components. The PDMS pressure block and the joint between PDMS L1 and PDMS mating layer are pressure fit. All other PDMS surfaces are permanently bonded.

The full package for the device is a glass-enclosed chamber, having interior dimensions of approximately 30 × 15 × 7 mm, which reduces noise caused by ambient air movement. The chamber walls are two 1 mm thick glass slides. These are clamped in a machined aluminum block, which provides support and mounting rigidity within the experimental setup. To make package reuse possible, and enable easy switching of device dies, a two-level PDMS fluidic delivery scheme is used. The die-level PDMS ("PDMS L1" in Figure 2.5) is approximately 1 mm thick, and has molded fluid channels 100 μm in height. It is bonded to the device die, and routes fluids from round 1 mm ports directly to the cantilever microchannel in/out ports. In order to connect to this layer, the front-side glass slide of the package is drilled with 1 mm through-holes (using a Dremel rotary tool), to match those in PDMS L1, and its inside surface is bonded to a ~1 mm thick PDMS "mating layer," also with matching 1 mm through-holes. The L1 PDMS is pressure-fit to the mating layer (the whole structure is pressed between the glass slides with a block of PDMS), providing a leak-tight seal. Because this junction is not a permanent bond, a

die can be removed and swapped out with minimal effort. The mating layer PDMS is necessary because simply pressing PDMS against the glass is insufficient and allows leaks. The alignment of all these layers is not critical since the features are mm-scale, and can be easily done by hand with the assistance of a stereomicroscope. Attaching the L1 PDMS to the die requires a little more care, but can be done in a similar fashion with 50-100μm accuracy (see Figure 2.6).

The second level of fluidics ("PDMS L2") is bonded to the outer surface of the drilled glass slide, and provides a connection from the tubing to the fluid ports through the glass leading down to the die. This layer is thicker (~3-4mm) to provide support for 1.09 mm O.D. polyethylene tubing (Intramedic PE20), which is inserted into 0.5 mm diameter holes cut in the PDMS. Since PDMS is highly compliant, the tubing seals snugly into these holes.

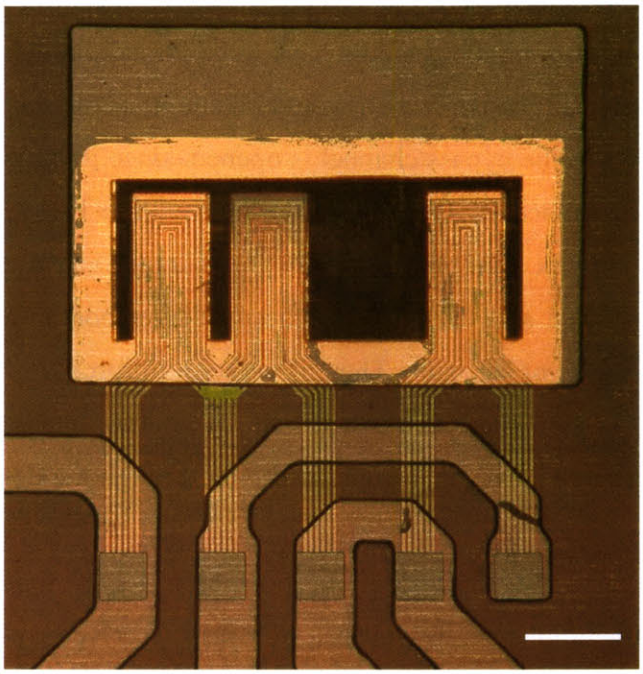

Figure 2.6: L1 PDMS attached to devices. Photo showing 100 μm PDMS fluidic channels bonded on top of the cantilever microchannel ports. Scale bar is 200 μm.

All holes through PDMS layers are cut on a Universal Laser Systems X-600 laser cutting system. Previously, holes through PDMS had been made by punching with a 16-gauge needle – an extremely imprecise and time-consuming serial process. The laser cutter provides enormous gains in speed, precision, and quality. Original CAD drawings from Cadence can be easily exported in a format compatible with the laser cutter, allowing fluidic layout to be done together with the device mask layout. Aligning the holes to existing fluidics molded in PDMS can be done with 100 μm accuracy by hand. Though the cutting process leaves a lot of residue on the PDMS, ultrasonic cleaning in isopropyl alcohol and water is sufficient to enable bonding and sealing of laser-cut pieces.

2.3.2 Fluid delivery

Since the very thin cantilever fluid channels have an extremely high flow resistance (only 0.5-1.0 μm high), the L1 PDMS channels connect to their in/out ports using a bypass configura-

tion (shown in Figure 2.7), which reduces the time needed for sample fluid to reach the devices. If the supplying PDMS channel were simply to terminate on the SiN_x port, in a straight-through connection, any fluid already in the channel and the comparatively enormous dead-volume in the connecting tubes would have to be forced through the cantilevers, which would take hours. Instead, when the bypass channel is opened, since its flow resistance is $\sim 10^4 - 10^5$ times lower, the PDMS network can be filled with the sample, and the desired analyte placed at the cantilever port in a matter of seconds. Then, if we wish to force flow through the cantilevers, we close the bypass channel, and the sample is driven through the devices.

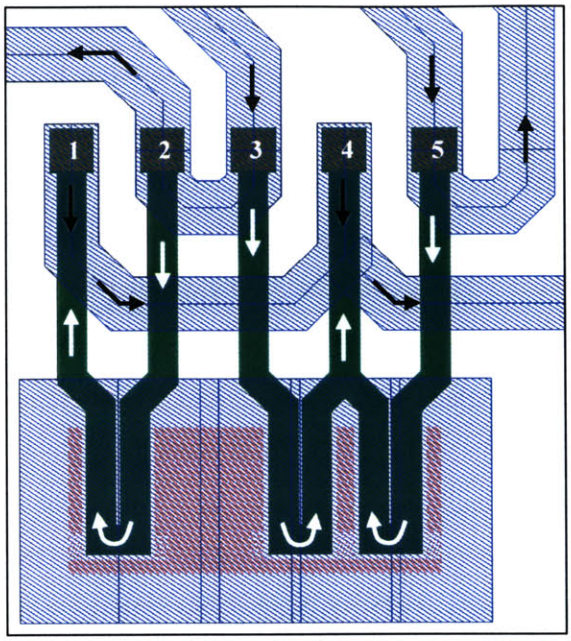

Figure 2.7: PDMS fluidic connections to cantilever ports. Blue areas are PDMS channels, green areas fluid channels in SiN_x, (taken from Cadence design layout) Black arrows indicate flow directions in PDMS, white ones show flow in SiN_x. Note bypass connection to all input ports (2, 3, 5) – sample is flowed in bypass mode to flush dead volume in PDMS. Output ports (1, 4) have a terminated PDMS channel, since fluid is never forced through cantilever channels this way.

Macro-scale fluid flow to the system is accomplished by means of pressure-driven syringe pumps connected to the tubing inserted into the L2 PDMS. We use low pressures of 5-10 PSI to drive the flow, in order to avoid high pressure forces, since it is not yet clear how much pressure the packaging can withstand before it leaks.

2.4 Fabrication

While the fabrication process development and its details are outside the main focus of this thesis, we briefly cover device fabrication here in order to provide some context for device features and parameters which will be described in later Sections. Fabrication is treated in greater detail in Appendix A.

The hollow cantilever devices were fabricated at the Microsystems Technology Laboratories (MTL) at MIT using standard micromachining techniques. In order to overcome the challenge of creating freestanding hollow structures with extreme aspect ratios, two different fabrication approaches were pursued in parallel in collaboration with T. Burg. The first, based on wafer bonding, was intended specifically for the hollow thermal sensor. The second, based on polysilicon sacrificial layer etching, was primarily meant for use in a resonant mass-sensor application, also using a hollow cantilever structure [19].

Both processes begin with an etch in silicon of the appropriate depth (~0.5-1.0 μm) to define the channel shapes, which are then conformally coated with low-stress SiN_x to form the bottom half of the device. The processes diverge in the steps used to attach and seal the top layer of nitride. For the bonded process, a second wafer, also coated with low-stress SiN_x is direct-fusion-bonded to create a "lid" for the hollow structures, after which the second wafer is etched away in KOH to expose the devices. Meanwhile, in the sacrificial process, a layer of polysilicon is deposited on top of the SiN_x layer and polished down (CMP) such that it only fills the channel trenches (Damascene process). The top layer of SiN_x is then deposited by CVD to close the devices.

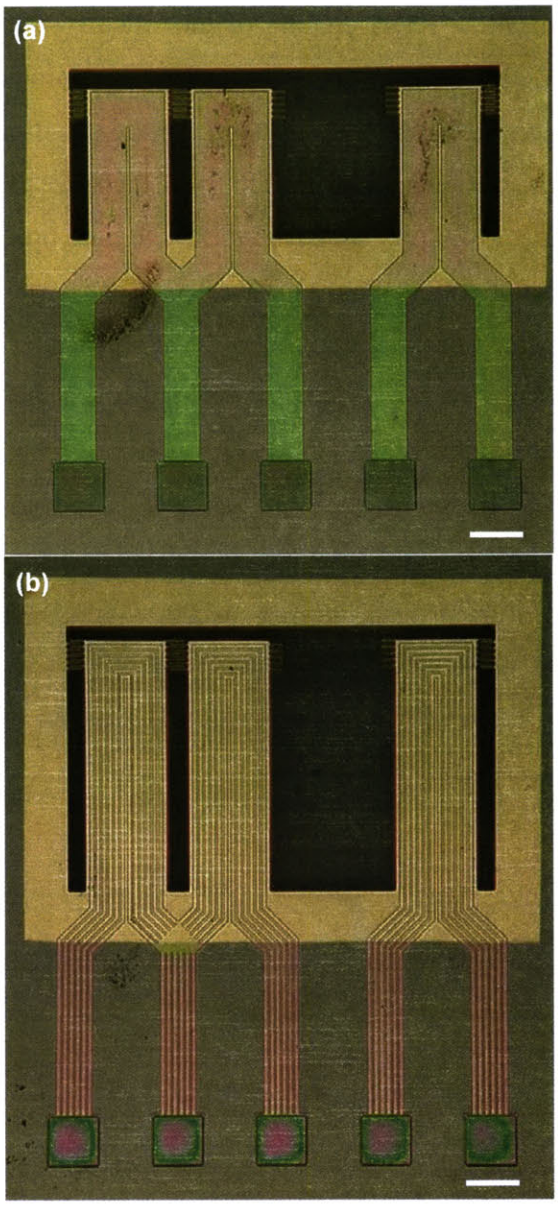

Figure 2.8: Fabricated device photos. (a) 300 μm cantilevers with one-piece channels and (b) 500 μm cantilevers with subdivided channels. Both were fabricated with 800 nm thick SiN_x, and 500 nm fluid layer height. The dark rectangular area is KOH-etched opening in die, into which cantilevers protrude. Note ID fingers, both absolute and differential. The fluid channels are covered by SiN_x, except at the square ports. White scale bars are 100 μm.

At this point, the two processes again follow the same steps, in which the joined SiN_x layers are patterned to define the device shapes, and openings are etched in the backside nitride

to allow KOH etching of the silicon wafer bulk in order to release the cantilevers. The final KOH etch step leaves the cantilevers protruding from the edge of the supporting silicon, and is carried out for a longer time in the sacrificial process to etch out the polysilicon and hollow out the channels. For the details of each process, see Appendix A.

After extensive work with both processes, the second proved much more successful, with around 80% yield. Figure 2.8 shows two different sets of devices resulting from this fabrication run. All experiments described in Chapter 4 were, therefore, performed with devices fabricated using the sacrificial process. However, the mask layouts and design details for the two processes are different, and not every feature of the successfully fabricated devices was specifically designed for thermal applications. In Chapter 3, many of the calculations and derivations apply equally well to devices fabricated using either process, and some analysis is done on features unique to each process. In particular, the option of adding a vessel to the cantilever tip is only possible using the bonded wafer process (a sacrificial layer is limited to a maximum thickness of 2 μm), while the subdivided U-channel modification is exclusive to the design used with the sacrificial process.

3 ANALYTICAL MODELING

Predicting the performance of the hollow cantilever sensor requires analysis in two key domains. First, we examine the thermally-induced bending of the device, based on purely mechanical considerations. Next, we work in the thermal energy domain to derive the temperature and heat flow profiles in the structure. We finally combine these models to predict the cantilever deflection that will result from thermal energy released by samples held within the device.

For the analyses that follow, we assume a simple hollow box structure for the cantilever, and refer to geometrical parameters as illustrated in Figure 3.1. Figure 3.1 (a) shows the coordinate system used in modeling cantilever deflection, with L_B representing the length of the bimorph section, and in figure 3.1 (b), which shows the beam cross-section, W is the cantilever width, and t_M, t_F, and t_N are the thicknesses of the metal, fluid, and nitride layers respectively (for all analyses that follow, we assume $W >> t_F$, and approximate accordingly). Similarly, material properties for the three layers are denoted by symbols with the subscripts M, F, and N referring to the metal, fluid, and silicon ni-

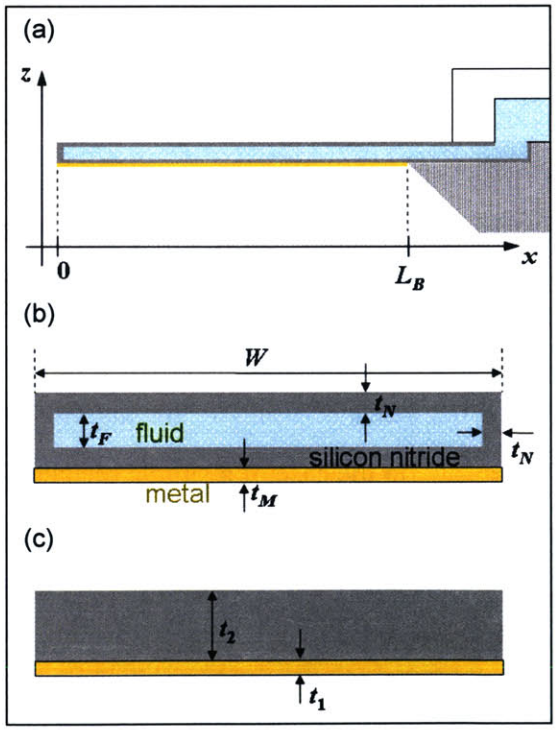

Figure 3.1: Cantilever analytical parameters. (a) Cantilever side-view cross-section showing coordinate system used for analysis. (b) End-view cross-section showing various material layer parameters. (c) Simple bi-material cross-section with no internal fluid channel.

tride layers, respectively. For mechanical analysis, $E_{[x]}$ are the elastic (Young's) moduli, and $\alpha_{[x]}$ are the coefficients of thermal expansion of the materials. For thermal analysis, $\kappa_{[x]}$ are the thermal conductivities, $\rho_{[x]}$ the mass densities, and $c_{[x]}$ the volumetric heat capacities.

Below, we carry out both the mechanical and thermal analyses, and combine them to obtain a full picture of thermally-induced bimorph bending in the hollow cantilever structure. We also examine the effect of the two major device variations on device performance: subdivided fluid channels and a vessel at the tip.

3.1 Mechanical Beam Bending

Using simple beam bending theory, for a simple two-material strip sandwiched together, as shown in Figure 3.1 (c), the curvature caused by a temperature change is derived by balancing strains and bending moments at the material interface, resulting in the following equation:

$$\frac{1}{\rho(x)} = \frac{d^2 z(x)}{dx^2} = \frac{(\alpha_1 - \alpha_2)}{\frac{h}{2} + \frac{2(E_1 I_1 + E_2 I_2)}{hW}\left(\frac{1}{E_1 t_1} + \frac{1}{E_2 t_2}\right)} \cdot \Delta T(x). \qquad (3.1)$$

Here, with x as the coordinate along the beam length (see Fig. 3.1(a)), curvature is denoted by $\frac{1}{\rho(x)}$, (where $\rho(x)$ is the radius of curvature at every point along the beam) or equivalently $\frac{d^2 z(x)}{dx^2}$, where $z(x)$ is the beam deflection. Also, in Eq. (3.1), $h = t_1 + t_2$ is the total thickness of the structure, and I_1 and I_2 are the cross-sectional moments of inertia of each layer, given by $I_x = \frac{W \cdot t_x^3}{12}$ in the case of a simple rectangular layer cross-section.

To analyze our hollow fluid-filled cantilever structure, we assume here that the fluid layer exerts negligible stresses within the structure, since the fluid can flow through its inlet/outlet ports in response to any strains resulting from cantilever deformation. We can therefore follow a parallel method of strain- and moment-balancing to arrive at a similar expression for the beam curvature due to thermally induced stress:

$$\frac{1}{\rho(x)} = \frac{d^2 z(x)}{dx^2} = \frac{(\alpha_M - \alpha_N)}{\frac{h_B}{2} + \frac{2(E_M I_M + E_N I_N)}{h_B W}\left(\frac{1}{E_M t_M} + \frac{1}{2E_N t_N}\right)} \cdot \Delta T(x), \qquad (3.2)$$

in which $h_B = 2t_N + t_F + t_M$ is the corresponding total cantilever thickness and the cross-sectional moment of inertia for the nitride box structure (gray in Fig. 2.1 (b)) is given by

$$I_N = \frac{W \cdot \left(4t_N^3 + 6t_F t_N^2 + 3t_F^2 t_N\right) + t_F^3 t_N}{6}. \tag{3.3}$$

It is noteworthy that the thermally-induced curvature has a very weak dependence on the elastic moduli of the materials, but is linear with the mismatch in thermal expansion coefficients between the two materials. This indicates that material α_M and α_N are the material properties that should motivate the material choice. Also evident is that the beam width has almost no effect on the mechanical response. We will shortly see that the key geometrical parameters that govern cantilever response are the various material layer thicknesses and the beam length.

3.2 Thermal Analysis

We would like to determine the temperature distribution $T(x,y,z,t)$ in the cantilever, which will result from heat generation within the fluid inside it. For the purposes of this analysis, we assume that the fluid is water, and treat it as being stationary within the device (rather than flowing through), with no forced convective heat transfer. We also assume convective and radiative losses from the cantilever to the surrounding air to be negligible, leaving us to consider heat transfer by conduction only, which will provide a good first-order approximation.

We take the heat flow equation as a starting point, and include the heat source term:

$$\rho_m c_m \frac{\partial T}{\partial t} = \kappa \cdot \nabla^2 T + \dot{Q}_{GEN}, \tag{3.4}$$

where $\dot{Q}_{GEN}$ is the heat power density (W/m^3) generated within the fluid, ρ_m is the mass density, c_m the volumetric heat capacity, and κ the thermal conductivity. In order to simplify the analysis, we assume uniform and steady heat generation throughout the fluid layer, boundary conditions of zero heat flow at cantilever-air interfaces, and a perfect heat sink at the cantilever base (constant temperature equal to the ambient, which we label as $T = 0$). We can further simplify the situation by assuming steady-state conditions for this analysis, setting $\frac{\partial T}{\partial t} = 0$ (we will motivate this assumption shortly when we consider transient behavior). Finally, we can reduce

the problem to only one spatial dimension: because the device is so thin, and due to its width-symmetry and boundary conditions, the temperature through any cross-section can be considered constant. Thus, the temperature profile only depends on x (the length dimension), and we end up with

$$\frac{\partial^2 T}{\partial x^2} = -\frac{\dot{Q}_{GEN}}{\kappa} \quad . \tag{3.5}$$

Solving this with the appropriate boundary conditions, with the cantilever tip located at $x = 0$, and the base at $x = L_B$, results in a parabolic temperature distribution

$$T(x) = \frac{\dot{Q}_{EFF}}{2\kappa_{EFF}}(L_B^2 - x^2), \tag{3.6}$$

in which we use $\dot{Q}_{EFF}$ and κ_{EFF} to represent the lumped "effective" heat generation and thermal conductivity, respectively. $\dot{Q}_{EFF}$ comes from scaling the generated power density by the fraction of the device cross-section in which it actually occurs, yielding

$$\dot{Q}_{EFF} = \frac{\dot{Q}_{GEN} t_F}{2t_N + t_F + t_M}, \tag{3.7}$$

whereas κ_{EFF} is obtained by adding in parallel the thermal conductivities of the three layers, which yields

$$\kappa_{EFF} = \frac{2t_N\kappa_N + t_F\kappa_F + t_M\kappa_M}{2t_N + t_F + t_M} \quad . \tag{3.8}$$

Therefore, the final expression for the temperature profile in terms of device parameters is

$$T(x) = \frac{\dot{Q}_{GEN} t_F}{4t_N\kappa_N + 2t_F\kappa_F + 2t_M\kappa_M}(L_B^2 - x^2) \tag{3.9}$$

To supplement our steady-state picture, we can also model some aspects of the sensor's transient behavior. Using lumped-element modeling of thermal conductivities and capacitances (see figure 3.2), we can obtain an expression for the thermal time constant of heat propagation along the length of the multilayer bimorph structure. In the circuit, each material layer is represented by a capacitance (from the heat capacity), and a conductance (the heat

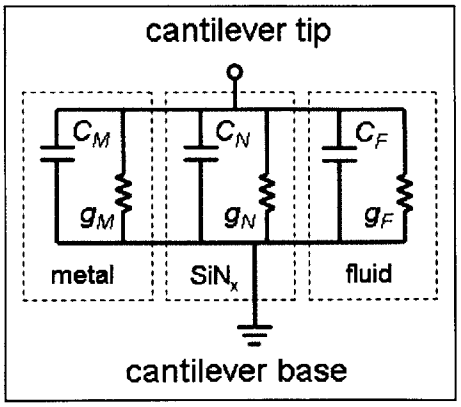

Figure 3.2: Lumped-element circuit model for transient thermal analysis.

conductivity), with heat flow represented by current and a temperature difference by voltage. Adding the capacitances and conductances in parallel, the time constant will be their quotient:

$$\tau_B = \frac{C_T}{g_T} = \frac{L_B^2(2\rho_N c_N t_N + \rho_F c_F t_F + \rho_M c_M t_M)}{(2t_N\kappa_N + t_F\kappa_F + t_M\kappa_M)}. \tag{3.10}$$

Note that the transient behavior is only weakly dependent on the layer thicknesses, such that process variations will have minimal impact on this aspect of device performance. This means that the layer thicknesses can be used to optimize thermally-induced bending performance, without adversely affecting sensor response time. In this analysis, we have assumed no heat transfer between materials, which is unphysical; however, this means our model provides a worst-case estimate for device response time, and the actual structure will have a faster time constant. With typical device dimensions, this model predicts time constants in the range between 1-20 ms. Even the slowest 20ms time constant is fast enough for many measurements, since the timescales of many biological events, such as reactions or binding events, happen over seconds or minutes.

Moreover, τ_B is only important for situations in which heat must be conducted along the entire length of the device – for example, if heating only happens at the tip of the cantilever (as in the case of the design with the vessel at the tip). If heat is generated uniformly throughout the device, the response is as fast as the time for heat conduction in the direction normal to the device layers (the z-coordinate) – from fluid sample out to the silicon nitride and metal. Since the device is so thin, this happens in 10s of nanoseconds, allowing extremely fast device response. These time constant calculations indicate that our initial approximation to consider only steady-state conditions was valid, since the device responds quickly enough to reach steady state with almost any thermal inputs it is likely to receive.

3.3 Cantilever Sensitivity

Having derived the thermal and mechanical behavior of the hollow beam structure, we can combine the two analyses to calculate the beam deflection that we can expect in specified conditions. Since we are interested in the deflection at the tip of the beam, which is where the ID interferometric measurement is made, the cantilever sensitivity is therefore defined as tip deflection resulting from a particular thermal input. To find this, we simply insert the appropriate temperature distribution into the equation for beam curvature, and solve for $z(x)$ at $x = 0$.

The simplest result that can be found this way is the ambient temperature sensitivity of the device – its response when the entire structure's temperature changes uniformly to a constant value. Inserting a constant for $\Delta T(x)$ into Equation (3.2), and integrating twice, we obtain

$$z(x)\Big|_{x=0} = \int_0^L \int_0^L \left\{ \frac{1}{\rho(x)} \right\} dx dx \Bigg|_{x=0} = (crv) \cdot \frac{L_B^2}{2} \tag{3.11}$$

where (crv) represents the curvature pre-factor on $\Delta T(x)$ in Equation (3.2). With the "default" set of parameters (see Section 2.2), the cantilever exhibits a sensitivity of 4.36×10^{-4} K/Å, which is a deflection of 229 nm per Kelvin change in temperature. Figure 3.3 shows the dependence of the temperature sensitivity on varying the key geometrical parameters of the device.

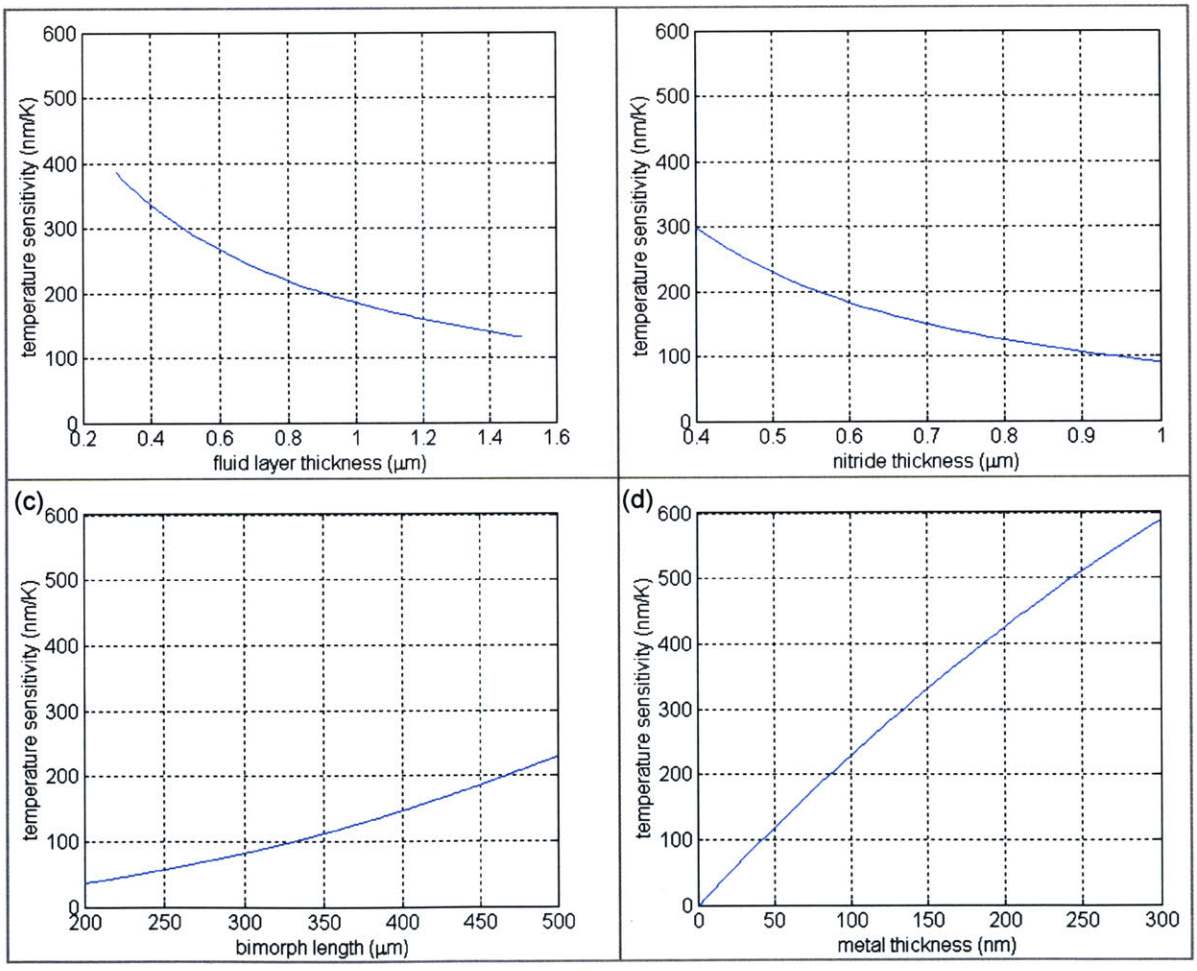

Figure 3.3: Cantilever temperature sensitivity. The plots show the effect of changing the fluid cavity height, SiN_x layer thickness, bimorph length, and metal thickness, in (a), (b), (c) and (d) respectively. As each parameter is varied, the others are held fixed at their default values: 500 μm long and 100 μm wide cantilever, 0.5 μm thick nitride, 0.75 μm thick fluid cavity, and 100 nm thick aluminum metal.

Since this device is intended for thermal measurements on samples contained within it, the sensitivity to heat power generated in the internal fluid volume is much more important than temperature sensitivity. We therefore substitute the parabolic temperature function $T(x)$ from Eq. (3.9) into the expression for beam curvature, and again integrate twice:

$$z(x)\Big|_{x=0} = (crv) \cdot \frac{\dot{Q}_{GEN} t_F}{4t_N \kappa_N + 2t_F \kappa_F + 2t_M \kappa_M} \cdot \frac{5L_B^4}{12}. \tag{3.12}$$

Here (crv) is the same curvature pre-factor from Eq. (3.2). Using Equations (3.2), (3.9) and (3.12) we can now examine the various dependencies of the device performance on the geometrical and process parameters.

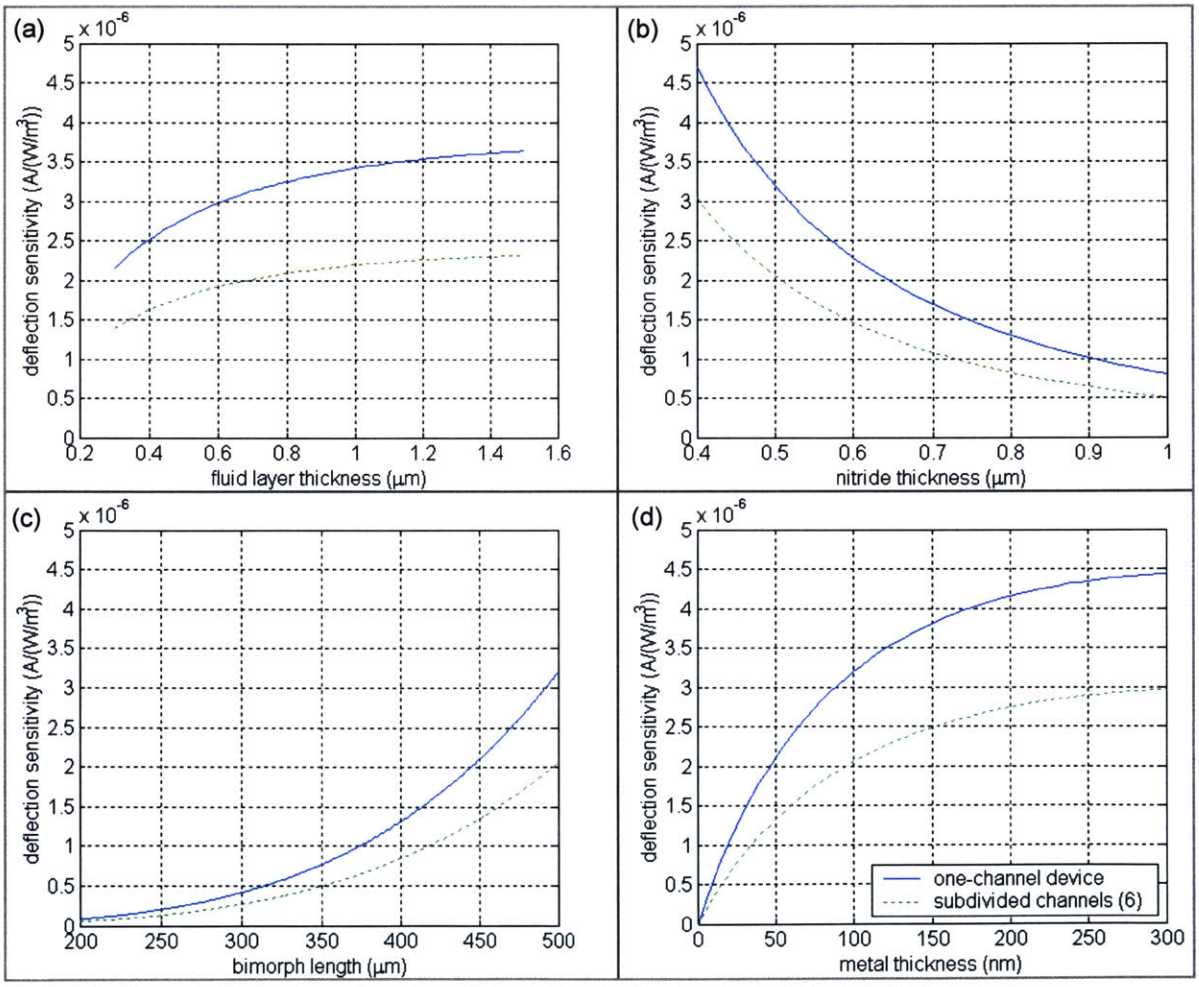

Figure 3.4: Parameter-dependent power sensitivity. As in Figure 3.3, non-varying parameters are held fixed at their default values. In addition, for all four plots, the solid curve shows calculations for cantilevers with single channels, and the dashed curve for cantilevers with six subdivided small channels (as in Figure 2.8 (b) and Section 3.4.1)

Figure 3.4 shows plots of device power sensitivity as functions of different parameters. These are instructive for determining which design parameters are most worth optimizing as a means of improving device performance. For example, doubling the fluid layer thickness from 0.75μm to 1.5μm gives only a 15% improvement in sensitivity, whereas halving the nitride layer to 0.4μm gives an over threefold improvement in sensitivity, and increasing the cantilever length from 300μm to 500μm increases it eightfold. It is natural that the cantilever dependence on bimorph length is so strong, since L_B has a fourth power dependence in the analytical expression.

Another key result to note is that when only the ambient temperature response is considered, increasing the fluid cavity height decreases the device sensitivity, since the greater sidewall height simply adds stiffness to the bimorph. However, when heat power is generated within the fluid, having a greater fluid volume is advantageous, and in the range with which we are concerned, the additional heat generation actually overcomes the increased stiffness, and a thicker fluid layer improves sensitivity[2].

3.4 Effects of Design Variations

We now briefly examine the changes in device performance that we can expect from the two design variations introduced in Section 2.2.2.

3.4.1 Subdivided fluid channels

We first consider the subdivision of the U-channel into smaller fluid channels. The actual cantilevers that were fabricated, as shown in Figure 2.8 (b) have the U-channel divided into six small ones, each 8 μm wide, with 4 μm dividers between them. This change effectively increases the number of sidewalls in the structure from four (with a single central divider between the arms of the "U" – top and left of Figure 3.5), to 24, shown at the bottom of Figure 3.5. Intuitively, we expect that these sidewalls will add stiffness to the structure, while small channels will decrease the total fluid volume within – both these effects will combine to decrease power sensitivity.

[2] Beyond the range shown in Fig. 3.4, increasing the fluid layer thickness further reaches a maximum sensitivity of 3.75×10^{-6} Å/(W/m^3) at 2.9 μm, slowly decreasing at higher fluid layer thicknesses. However, such large fluid layers are never fabricated.

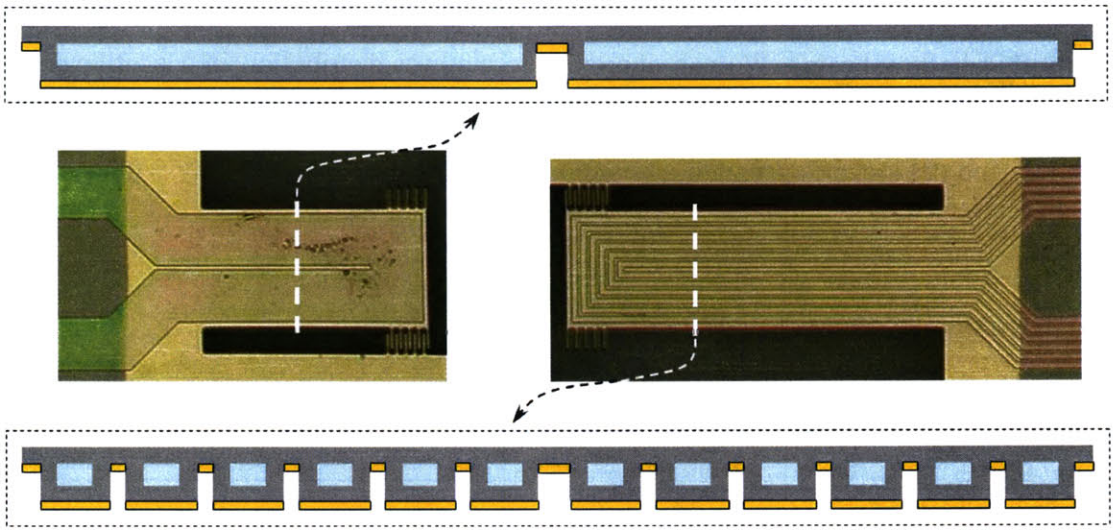

Figure 3.5: Subdivided fluid channels. Schematic cross-sectional views are shown at the top and bottom for the one-piece channels (top and left), and the subdivided channels (bottom and right), with nitride, fluid and metal layers shown. Vertical dimensions in drawings are exaggerated.

Analysis indicates that the increased stiffness from the extra sidewalls contributes only a negligible effect, and the power sensitivity reduction is caused primarily by the reduced volume within the structure. With the channel subdivided into six, the volume inside the cantilever is reduced by approximately 30%, and the overall reduction in power sensitivity is approximately equivalent. This is illustrated on the plots in Figure 3.4 with dashed lines. The lowered sensitivity resulting from this modification is likely worth the improvement in yield, especially with the longest devices – 500 μm cantilevers with one-piece channels have only about a 50% yield, whereas subdividing the channel increases it to essentially 100%.

A less predictable change within the structure caused by subdividing the fluid channel is the effect on fluid flow resistance. With the subdivided channels, the increase in flow resistance is only about 45%, based on lumped-element Poiseuille flow calculations. However, smaller fluid channels are more susceptible to blockage, and more sensitive to variations in channel dimensions. It is not yet clear which of these effects is dominant, and subdivided fluid channels may prove useful and necessary in some situations.

3.4.2 Tip Vessel

The second major design modification under consideration is the addition of a vessel to the cantilever tip. The intention is to increase the total fluid volume capable of generating ther-

mal energy, which will then be conducted through the sensor to give a larger signal than a simple uniformly thin hollow beam. We can approximate the heat distribution in a cantilever with a vessel using a superposition of two solutions: (1) a sensor with no vessel (already treated in the Section 3.2) and (2) a cantilever with a vessel with heat being generated only within the vessel volume.

In the latter case, we consider heat generated within the bimorph section to be negligible in comparison to that generated within the vessel. This is true in cases of interest to us, since the purpose of the vessel is to overwhelm the heat generated in the bimorph. Referring to the coordinate system and dimensions in Figure 3.6, and applying the appropriate boundary conditions, we solve the heat flow equation once again, and obtain a linear temperature distribution through the bimorph described by

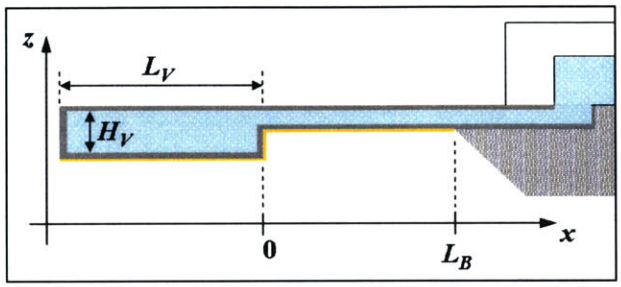

Figure 3.6: Coordinates and dimensions for a cantilever with a vessel. In this scheme, the cantilever tip is located at $x = -L_V$.

$$T(x) = \frac{\dot{Q}_{GEN} \cdot H_V L_V}{\kappa_{EFF}(2t_N + t_F + t_M)}(L_B - x) \ , \tag{3.13}$$

where we take the $x = 0$ to be at the junction between the vessel and bimorph sections, and the cantilever tip is at $x = -L_V$. Note that the temperature distribution of Eq. (3.13) is valid only for $0 < x < L_B$. Using this temperature profile in the curvature Equation (3.2), and integrating twice, as before, the resulting power sensitivity expression is:

$$z(x)\big|_{x=0} = (crv) \cdot \frac{\dot{Q}_{GEN} \cdot H_V L_V}{\kappa_{EFF}(2t_N + t_F + t_M)} \cdot \frac{L_B^3}{3} \ . \tag{3.14}$$

Using this function, we can extrapolate from the slope at the bimorph-vessel junction to derive the beam tip deflection at $x = -L_V$. For a 500μm long device without a vessel, the power sensitivity is $\sim 3\times10^{-6}$ Å/(W/m^3), whereas by making the outer 200 μm of the beam a 50 μm deep vessel, we can reach $\sim 6\times10^{-5}$ Å/(W/m^3) – a twenty-fold increase in signal magnitude. Figure 3.7 demonstrates the benefits of adding a vessel to the cantilever tip. The trade-off between a longer vessel and a shorter bimorph is evident, and it is clear that the vessel length that gives the best signal increase is approximately 36% of the total cantilever length.

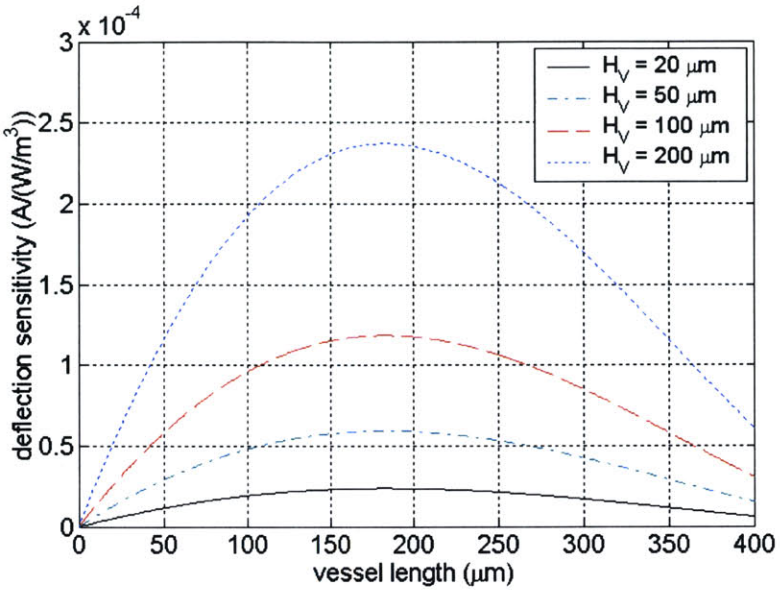

Figure 3.7: Effect on device power sensitivity of different vessel sizes. For all curves, the total cantilever length is held constant at 500 μm, while the bimorph section length is varied correspondingly with the vessel length (e.g. with a 150 μm vessel, the bimorph is 350 μm long).

3.5 Potential Applications

3.5.1 Minimum detectable deflection

The minimal detectable deflection (MDD) signal of this cantilever sensor system is equal to the noise present in the system. Before the experiment is actually running, we can estimate the noise-limited resolution from experience with similar devices. In particular, the differential cantilever system used by Savran *et al.* has the noise characteristics in air shown in Figure 3.8 [16]. While the performance of the hollow cantilever will no doubt be different, the device geometries are similar enough

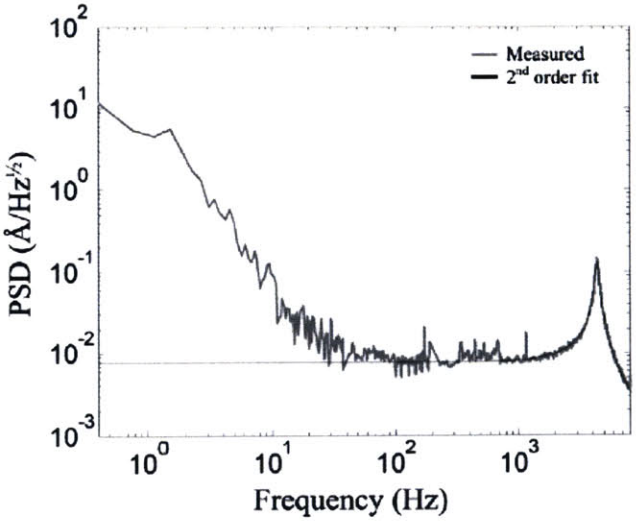

Figure 3.8: Noise power spectrum of differential stress sensor fabricated by Savran *et al* (reprinted with permission from [16]).

for this to provide insight into the types of measurements of which the hollow cantilever will be capable (in section 4.3.1 we re-visit the accuracy of this assumption).

3.5.2 Possible thermal experiments

If we are interested in real time calorimetric measurements of biological reactions, these occur over timescales of seconds or minutes. Unfortunately, at frequencies of 1 Hz and below, our device requires a deflection greater than 1 nm for a signal to be detectable. The power density required to give such a signal is on the order of 10^6 W/m^3, even for the most sensitive combination of device parameters. In biological reactions, such a power density is extremely unlikely, and possible only for very energetic reactions, at very high concentrations. For instance, Johannessen *et al.* measured the breakdown of hydrogen peroxide by catalase in their nanocalorimeter [4]; this reaction is one of the "hottest" in biological systems, and at concentrations of ~10mM their reaction reached ~10^6 W/m^3. Clearly, under physiological conditions (i.e. with lower concentrations and tamer biochemistry), power densities are much lower, and detection using the hollow cantilever is unfeasible.

A type of measurement that does appear promising, however is photothermal spectroscopy. As already mentioned, some photothermal measurements using flexible microcantilevers have already been reported [6, 12], but these have used samples adsorbed to a dry cantilever surface exposed to air, with no inherently differential readout. This type of measurement would be interesting to carry out using the hollow cantilever system, which provides far better control over sample delivery, and maintains a liquid environment. Detection is easier in this type of experiment for two reasons. First, since pulsed modulation of the light source is possible, we are able to operate the device at 50 Hz and above, where the noise power density is three orders of magnitude lower than near DC. Secondly, high power density is achievable in a photothermal experiment by using high analyte concentration and illuminating with a high-power light source. Preliminary calculations indicate that a power density of 10^6 W/m^3 is achievable, and should be easily detectable at noise levels of ~0.01 Å/Hz$^{1/2}$. We present more detailed calculations in the next chapter, together with experimental results.

4 EXPERIMENTAL

In order to demonstrate the functionality of the device, it has been used to perform a photothermal spectroscopy measurement. Based on simulation results, and knowing the typical noise levels expected with our instrumentation and experimental setup, we hypothesized that such a measurement should be possible with the hollow cantilever sensor. This chapter describes principles of photothermal spectroscopy, the experimental setup, and some initial results.

4.1 Photothermal Spectroscopy

This is a sensitive analytical method used to study the optical and thermal properties of a sample. Its aim is essentially to observe the changes in the thermal properties of a sample that result from a temperature shift induced by photo-absorption. This method is, in a way, a more accurate measure of absorption than spectrophotometry. The latter method measures transmission, and does not account for reflection, scat-

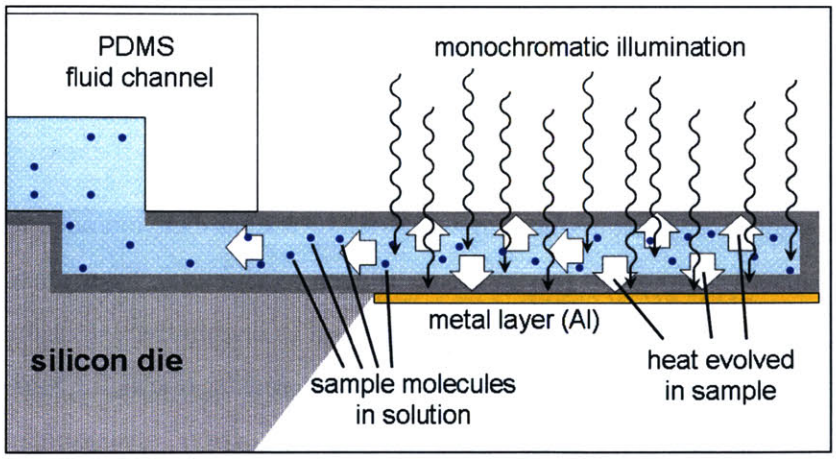

Figure 4.1: Photothermal spectroscopy schematic. Monochromatic illumination passes through the nitride and some energy is absorbed by molecules in the fluid within. This energy is converted to heat, which is conducted outward through the layers of the structure, as well as along the cantilever toward the substrate.

tering, or re-emission of light energy (as in fluorescent molecules, for instance), whereas photothermal measurements only measure energy absorbed and converted to heat. Generally, a photothermal spectroscopy experiment uses a variable-wavelength monochromatic light source to excite the sample. The excitation wavelength-dependent absorption can be observed by various means, including optical, pressure, or temperature sensors. With optical readout a laser is most often used, as is the case in our experiment. The resulting signal is filtered, processed and recorded.

Interestingly, Bialkowski notes in the preface his monograph on photothermal spectroscopy methods, "... there are no commercial photothermal spectrometers. All wishing to use photothermal spectroscopy must construct their own apparatus" [3]. Typically, in such an apparatus, refractive index changes or pressure waves resulting from sample fluid heating are detected. These measurements have high sensitivity, sometimes detecting only a few absorbing molecules in the sample.

The smallest volumes for photothermal measurements are usually microliter-scale. However, the sensitivity and signal strength are enhanced in smaller volumes, so a nanoliter-scale photothermal spectrometer is a promising direction of inquiry. The hollow microchannel cantilever is promising for use with photothermal spectroscopy, with the potential to improve upon the photothermal absorption measurements using microcantilever sensors that have already been reported [6, 12].

4.2 Experimental Details

4.2.1 Experimental setup

As described earlier, the cantilever sensor is held in a dual-window chamber, intended to give optical access to both the top and bottom surfaces of the cantilever, as shown in Figure 2.5. The transparency of packaging materials like PDMS and glass is crucial to enable the use of the two illumination sources required for photothermal spectroscopy measurements: one is the variable-wavelength monochromatic excitation beam, and the other is the deflection measurement laser. The monochromatic light source is a 175W xenon lamp (CVI Laser Y1603) aimed through a computer-controlled monochromator (CVI Laser CM110), which uses a 600 μm slit to only pass light within a narrow spectral band only 4 nm wide. The narrow-band light is output

using a 2 mm fiber-optic bundle, after which it is focused to a ~1 mm diameter spot to illuminate the cantilever pair. Since this light source does not have stringent focusing and positioning requirements it can pass through the thick layers of PDMS to strike the devices from the front (top side in Figure 2.5). This is in contrast to the measurement laser, which demands much more precise focus and minimal optical distortion, and is therefore passed only through a single glass slide. The aluminum layer on the back side of the devices simultaneously provides a reflective surface for the measurement laser, and allows the excitation beam from the front to pass through the transparent silicon nitride and reach the fluid inside the cantilever (in fact, reflections of this light off the backside aluminum can pass back through the sample fluid, boosting the signal).

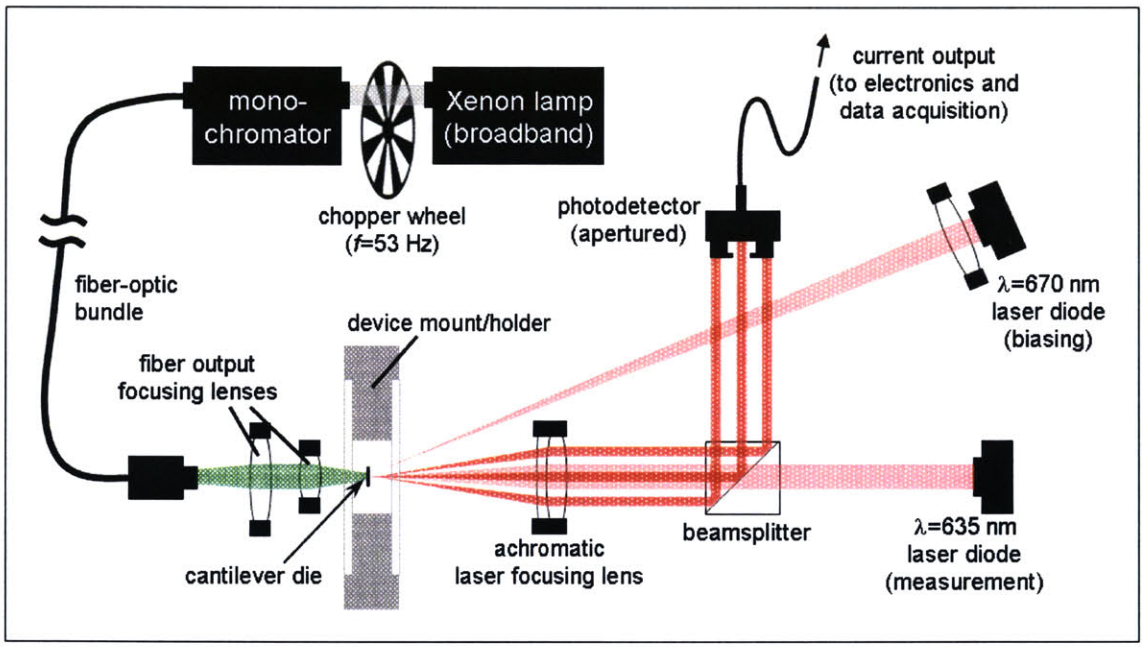

Figure 4.2: Optical system for photothermal spectroscopy experiment. Note three main components: (1) measurement laser and detector (2) biasing laser, (3) chopped monochromatic illumination

The optical measurement system for the experiment is set up as shown in Figure 4.2. A 3 mW measurement laser (Thorlabs DL3148-021) with $\lambda = 635$ nm is collimated and sent through a beamsplitter on the way to the device. It is focused onto the ID fingers of the cantilevers through a 60 mm focal length achromatic doublet lens, which is mounted on an x-y-z micrometer positioning stage, allowing precise alignment of the laser spot. The diffractive modes are reflected off the ID grating, back through the achromatic lens, and are steered by the beamsplitter onto the detector photodiode. An iris aperture is used to select only one (spatially station-

ary) mode onto the detector. The mode's intensity modulation is recorded and translated into equivalent cantilever deflection, which provides a measurement of the thermal power generated in the cantilever.

From the detector, the optical signal becomes electronic, as the diode outputs a photocurrent proportional to the intensity of the incident laser mode. This current is passed across a 100 kΩ resistor and into a pair of voltage pre-amplifiers (Tektronix AM502), which are used to provide a moderate gain (5x), control the signal offset, and high-pass filter it to minimize the effects of low-frequency drifts and disturbances. The signal is then passed to a lock-in-amplifier (Stanford Research Systems SRS830) for narrowband measurement (see section 4.2.3 below), and finally into a LabVIEW (National Instruments) computer-controlled data acquisition system for data recording. A LabVIEW "virtual instrument" (VI) is used to sequentially step the monochromator output wavelength through a specified range, sample and average the lock-in amplifier's output at each step, and store the data.

4.2.2 Biasing

An important element required for properly controlled measurement is a means of controlling the bias point at which the cantilever operates. The intensity of each mode I has a nonlinear dependence on the relative out-of-plane finger displacement d, of the form $I \propto \sin^2\left(\frac{2\pi d}{\lambda}\right)$, such that for a finger displacement equal to ¼ wavelength of the illumination laser, one mode's intensity modulates from zero to full brightness. To achieve maximum deflection sensitivity, the device needs to operate where the slope of this function is greatest – midway between the maximum and minimum. Unfortunately, due to stresses and other device variations resulting from the fabrication process, it is impossible to precisely control the relative position of the two cantilevers' ID finger sets at equilibrium, so the device's inherent bias is unpredictable. However, we can use a second laser to deliver a precisely controlled amount of heat to one of the cantilevers, bending it as needed to the desired bias point. For this

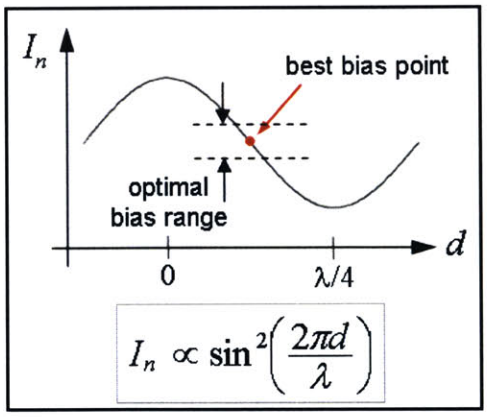

Figure 4.3: Biasing characteristic of ID mode readout.

we use a $\lambda = 670$ nm, 10 mW laser (Toshiba TOLD9225) driven by a variable-current laser driver (ThorLabs LDC500), focused at the base of one of the cantilevers.

In addition, by modulating this bias laser to swing the mode intensity through its full range, and recording the slope at the bias point, we can calibrate our measurement, enabling us to correlate output voltage to nanometers of deflection at the bias point. Significantly, the stability of this bias point has an important effect on the final measurement: since the output characteristic is nonlinear, deviations from the bias point cause corresponding fluctuations in the slope. Keeping the bias drift constrained to within 10% of full swing ensures that the error in slope is less than 1% [24]. Typically, over the timescale of a single photothermal experiment (3 min or about 5 mHz) the noise is low enough that the bias easily remains within this range (e.g. at 1 mHz, the noise in Savran's devices is 10 nm/Hz$^{1/2}$, while 10% of full swing is 16 nm).

4.2.3 AC measurement

In order to minimize the effects of noise in our measurement system, we follow the example of many previous photothermal measurements [3, 6], taking advantage of the device's rapid thermal response to optical excitation (see section 3.2), and combine pulse-modulated illumination with phase-sensitive lock-in amplification to narrow the measurement bandwidth. Before entering the monochromator, the excitation light source is modulated using an optical chopper wheel (Thorlabs MC1000) at a frequency of 53 Hz, creating a square-wave pulsed optical excitation signal. The chopper's synchronous electronic output is used as the reference input into the SRS830 lock-in amplifier, which only amplifies a narrow bandwidth around the 53 Hz reference frequency. This effectively eliminates all noise components outside this narrow band; therefore, assuming satisfactory bias stability, the measurement resolution is only limited by the noise power density at 53 Hz, which is ~10^{-2} Å/Hz$^{1/2}$.

4.3 Results

This section discusses some initial experimental results, demonstrating the operating characteristics of the differential hollow cantilever sensor, and a proof-of-principle application to photothermal spectroscopy. It is clear that there is much that can be still be improved, and this is discussed in Chapter 5.

In this section, unless noted otherwise, all experiments that are described were done with a pair of 300 μm long single-channel cantilevers, with 800 nm nitride, 500 nm fluid layer, and 60 nm of aluminum on the back side. The monochromator was used with a 600 μm slit, and the lock-in time constant was set to 100 ms. The LabVIEW VI acquired data in the range of illumination wavelengths between 350 and 700 nm, in increments of 2 nm, pausing for 0.5 sec between steps, sampling each data point at 1 kHz and averaging 500 samples.

4.3.1 Absolute and differential spectra

We first demonstrate the ability of the differential cantilever pair to reject common-mode signals coming from both cantilevers. Figure 4.4(a) compares the differential spectrum of a pair of empty (unfilled) devices to the absolute spectrum of one of the cantilevers. The differential spectrum is featureless, and shows a 10-fold reduction in signal compared to the absolute deflection. The peaks in the absolute spectrum result from variations in incident light power, as well as absorption in the silicon nitride layers, which have previously been observed to give absorption spectra of this shape (data not shown). These background effects are effectively cancelled by using the differential readout, as intended, and the flat spectrum is noise-limited. This is evident from comparing the differential spectrum in Figure 4.4(a) to the spectrum in Figure 4.4(b), which shows the noise measurement of the differential readout, with the monochromatic illumination turned off (this noise measurement was taken with a different device of the same type, and with the lock-in time constant at 30 ms, which accounts for the higher variability in the signal). The noise magnitude is ~0.002-0.003 nm, which is comparable to Savran's measured noise PSD of 0.001 nm at 50 Hz. This suggests that hollow cantilever noise estimates using Savran's device's noise characteristics as predictors of hollow cantilever performance, are justified.

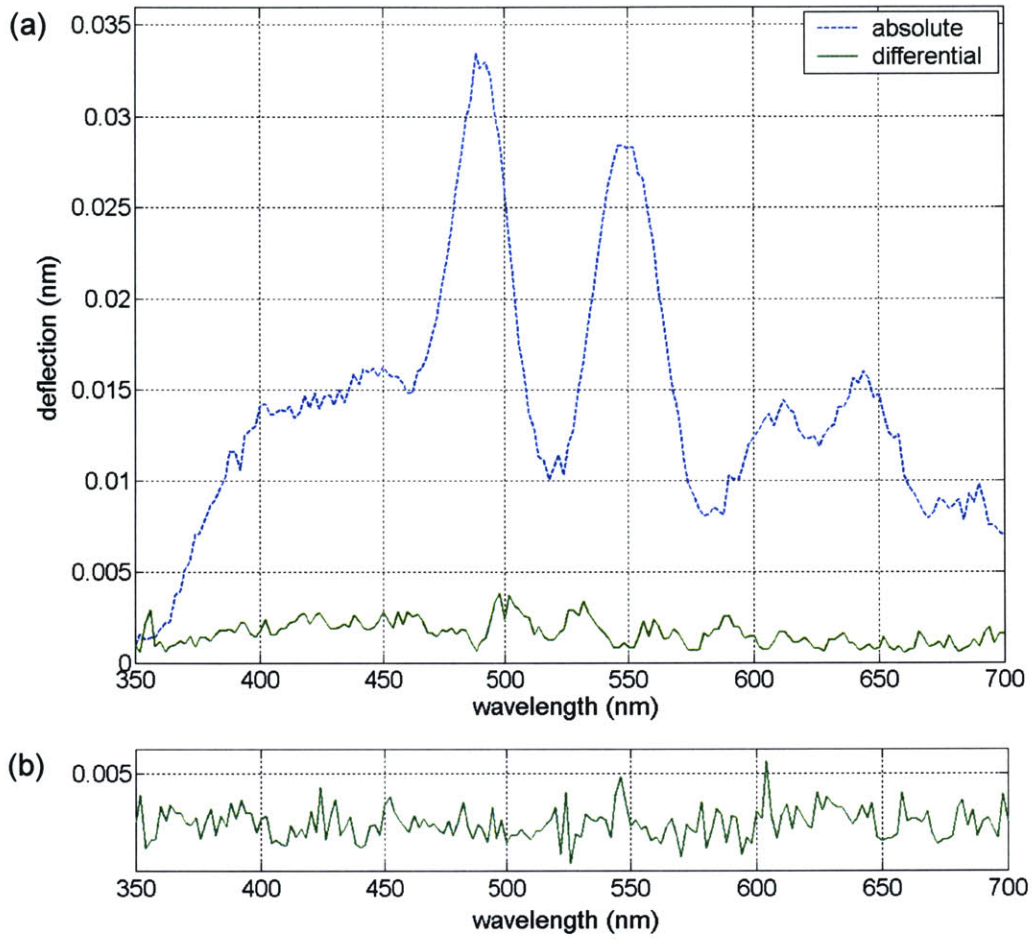

Figure 4.4: Empty cantilever spectra. Measurements taken on 300 μm long devices, before filling with sample. (a) Differential vs. absolute deflection. (b) Noise spectrum taken with the monochromator illumination switched off.

4.3.2 A dye absorption spectrum

As a demonstration of the ability of the hollow cantilever to act as a thermal sensor, we present here a photothermal spectrum of the dye proflavine (3,6-diaminoacridine hydrochloride) dissolved in water, recorded with the hollow cantilever. This measurement was taken differentially using the forced flow regime – both cantilevers' bypass channels were stopped – flowing de-ionized water through one of the cantilevers, and the proflavine solution through the other. We now examine some of these results.

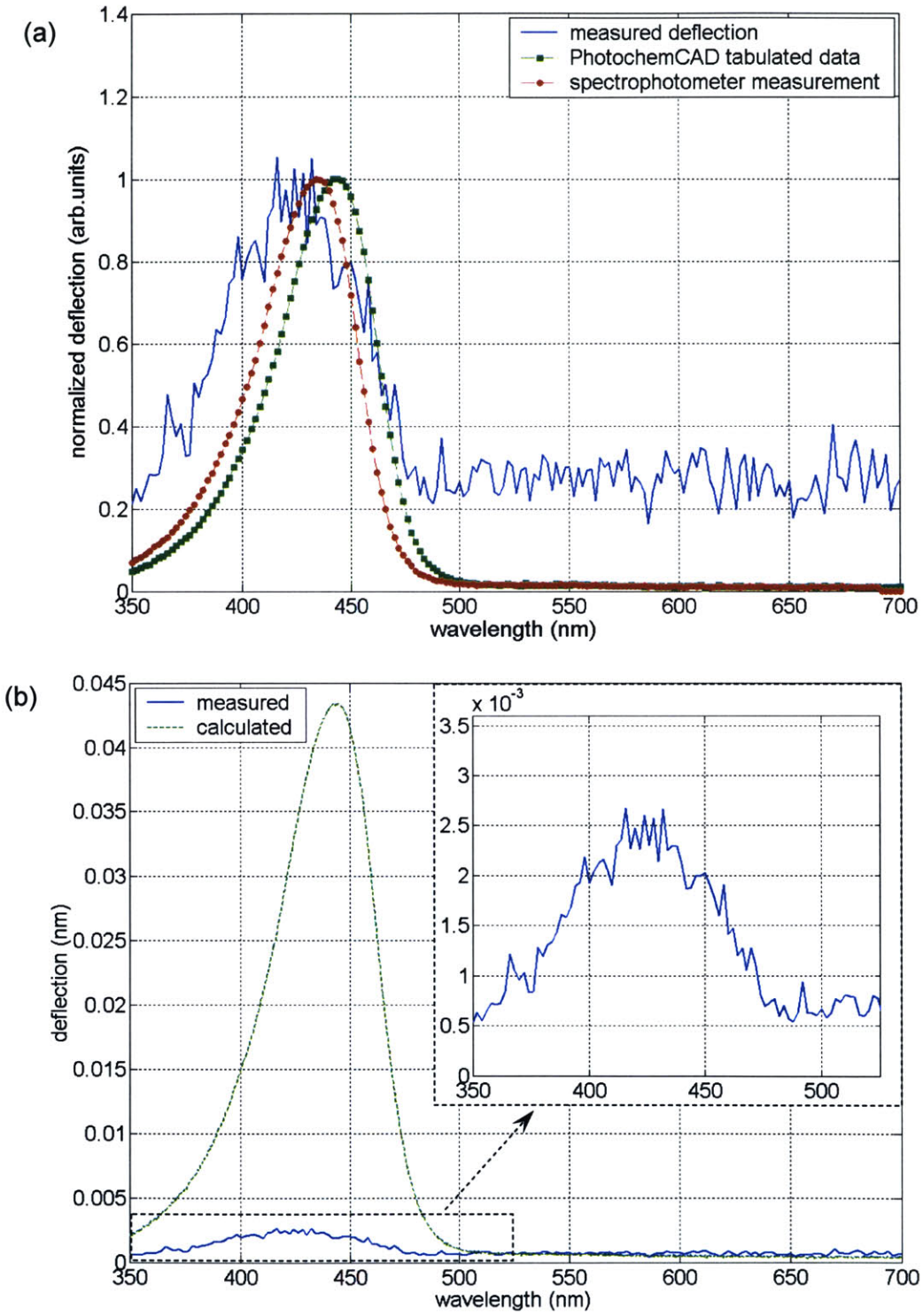

Figure 4.5: Proflavine absorption spectra. (a) Absorption curves, normalized by peak value, from device measurement, compared with two known data sources: PhotochemCAD database, and a transmission spectrophotometer measurement. Peak values are at 425, 445 and 435 nm, respectively. (b) The measured absorption spectrum compared with a theoretically calculated peak (appropriately scaled PhotochemCAD data).

Figure 4.5 (a) shows the normalized absorption spectrum data, shown in comparison to two known optical absorption spectra for proflavine, one from the PhotochemCAD photochemistry database [25, 26], available from the Oregon Medical Laser Center, and the other from a spectrophotometer absorption measurement done at MIT's Center for Environmental Health Sciences (CEHS). The peak width and location show good agreement with the optical data. The peak of our measured spectrum is centered at 425 nm, compared to 435 nm and 445 nm for the known data. Interestingly, the chemical supplier Sigma-Aldrich states in its catalog that the absorption peak of this compound is 456 nm. With this much variation in existing data, and accounting for the possibility of a calibration offset in the monochromator, we can be confident that the data in Figure 4.5 is a true absorption measurement. It is important to stress that the comparison data are purely optical measurements based on transmission; they are not photothermal spectra, so we should not necessarily expect what we observe with our cantilever sensor to exactly match this.

Finally, worth noting is the lower noise floor present in this measurement than what has been observed thus far. The peak in this spectrum is at a deflection of 2.5 pm (.0025 nm), which would be lost in the previously observed ~3 pm noise, whereas here we achieve a signal-to-noise ratio (SNR) of about 4, with a noise floor of ~0.7 pm, which is about four times lower than before. Preliminary data suggest that, when filled with fluid under steady pressure, the hollow cantilevers may exhibit lower thermomechanical noise than when they are empty, but more measurements and analytical modeling are necessary to verify this and determine its causes.

While the location and shape of the absorption peak correlate well with known data, the true magnitude of the cantilever deflection in this measurement is far below what would be expected with the experimental parameters. The expected cantilever deflection has been calculated and plotted together with the deflection data in Figure 4.5 (b). The expected deflection is found by determining the equivalent generated heat power density in the device, and inserting it into the analytical model from Chapter 3 to obtain deflection. According to the Beer-Lambert law, the transmitted intensity of light passing through an absorptive sample is given by $I = I_0\, 10^{(-\varepsilon c \cdot L)}$, where I_0 is the incident intensity, ε is the molar absorbance of the sample, c the sample concentration, and L the path length. Proflavine has an absorbance peak of $\varepsilon = 3.9 \times 10^4$ 1/(M·cm) at 445 nm, the solution used in the experiment is 10 mM, and, assuming a path length of 0.5 μm (one pass through the fluid layer, without reflections), we find that only about 4.4% of the incident

light power is absorbed by the sample. Scaling the monochromator output power of 40 μW at 445 nm by the fraction of the beam area intercepted by the cantilever, and by the absorbance factor, we find the total absorbed power to be 0.1 μW. Dividing by the total fluid volume of 22.5 pL (2.25×10^{-12} m^3) we obtain an equivalent power density of 4.5×10^6 W/m^3. The sensitivity of the cantilever being used is 9.6×10^{-9} $nm/(W/m^3)$, which gives an expected deflection of 0.043 nm at λ=445 nm.

The measured signal is about 20 times lower, and there are several likely causes. The most significant of these is the fact that the outlet channels of both cantilevers are joined, (as seen in Figures 2.3 and 2.8) allowing diffusion of dye backward from the junction, out of the sample cantilever, and into the reference one. Thus, we are likely detecting a difference in concentration between the two cantilevers, which is much smaller than the actual concentration of dye in the sample. The measurement is further degraded by the fact that conditions in the two cantilevers are not sufficiently the same for a true differential measurement. Contributing to this effect is the asymmetry of the fluidic connections to the input ports of the sample and the reference cantilevers (see Figure 2.6). This plays a role in making both the bypass fluid flow rate, as well as the cantilever through-flow, very unequal, further degrading the inherently differential character of the measurement.

Another possible effect could be transport of the generated heat out of the cantilever by the fluid flowing through it, before the heat can bend the device. However, at the low pressures used in this experiment, the fluid flow velocity through the cantilevers is at most 20 μm/sec, making it highly unlikely that this appreciably affects heat transfer properties. In fact, due to rapid heat transfer through the device layers (see Section 3.2), the flow speed can be increased 100-fold without having an effect on thermal behavior, and may even help to overcome the diffusive mixing mentioned above. We discuss more potential improvements to thermal experiments with these devices in the next chapter.

In summary, the sensor at least partially meets the original goals of achieving sensitive low-sample-volume, high-throughput thermal measurement. The device sensitivity is only mediocre, but can certainly be further optimized. The sample volume is near the lowest practical limits for a device through which the sample must pass (rather than simply resting on the sensor). Finally, the device throughput shows potential, and rapid sample switching is achievable with slightly more sophisticated microfluidic networks.

5 FUTURE WORK

Continued work on the hollow cantilever thermal sensor has three main phases. First, within a several-week timescale, a number of follow-up experiments can be done, both with devices already available and fabricated, as well as with those currently in progress through the fabrication process. Second, on a timescale of several months, the measurement system can be fine-tuned at the design level, and a new generation of devices fabricated, incorporating the design enhancements. Finally, new experiments can be performed with the new device generation, pushing the measurement system to its resolution limits.

5.1 Follow-up Experiments

A number of experiments can be carried out almost immediately with the sacrificial polysilicon design (Figure 2.3(b)), using devices from wafers which are nearly completed, except for KOH release. Because the cantilever pairs in this design all share a common outlet channel, it is difficult to achieve complete separation of the measured and reference sample. However, there are existing fluidic designs that have better-matched flow resistance and geometry than the device used for the measurements described in Chapter 4. This will enable better differential measurement, and with higher flow rates to mitigate diffusive mixing, the system will produce a better photothermal signal. In addition, more complete noise characterization can be performed, comparing both absolute and differential noise levels in unfilled devices with those flowing water under steady pressure. Finally, system calibration experiments can be performed by flowing water of different temperatures through the cantilevers and observing their bending.

To add to these experiments, devices with separated fluidic paths for each cantilever in a differential pair are currently in fabrication. The design originally used with the wafer bonded process (Figure 2.3(a)) is being fabricated using the sacrificial process. This process is just as well-suited to this design, which has excellent symmetry and well-matched PDMS fluidic connections. These devices emerging from fabrication will shortly enable further experiments with a refined photothermal system.

5.2 Next Generation System Improvements

Changes to improve the measurement system can be categorized into three broad areas: the fabrication process, the device design, and the fluid delivery system. All three are crucial factors contributing to device performance, and developing them can lead to numerous significant improvements for the measurement system.

5.2.1 Fabrication process

Since the sacrificial polysilicon process is largely successful, changes to it can be aimed at improving yield and device quality. In particular, the anisotropy of the final KOH release needs to be improved to minimize device and die undercut during the long sacrificial etch step. Also, longer devices have a tendency to crack when the fluid channel is one-piece, which is likely caused by stresses in the nitride layers, and generated during KOH release. These issues need to be addressed to produce more long devices, which show the best sensitivity.

One extra processing step is worth investigating, which may help to improve resulting devices after fabrication is completed. Hydrofluoric acid (HF) etches silicon nitride extremely slowly, and can be used to carefully thin the structural nitride of the cantilever sensors both from the inside and the outside. This can increase the internal fluid volume, while thinning the enclosing walls, both of which will raise device sensitivity. This is potentially a means of improving yield as well, since structures can be fabricated with thicker nitride to be more robust during release, and later thinned to reach high sensitivity.

5.2.2 Device design

This area of improvement includes any work to be done with the silicon wafer-based geometry and layout of devices, and involves re-designing the photomasks used for fabricating the sensors. The most obvious change to be made to the device layout, which will likely have the greatest impact on performance, is separating the fluid systems of the two adjacent cantilevers in a differential pair. When the two devices no longer share a common channel, the experimental and reference samples will not mix, and the full magnitude of the photothermal signal can be observed. In addition, device layout on the chip should be designed in conjunction with attached fluidics to properly match devices in a differential pair to each other (more on this in the next section). Finally, cantilever and wafer through-hole geometry should be optimized to enable absolute deflection measurement of each device in a pair, as well as differential measurement between them, allowing complete characterization of device operation.

5.2.3 Fluid delivery system

From the results of experiments using the existing differential hollow cantilever setup, it becomes clear that for true and effective differential measurement, it is insufficient to only match the pair of cantilevers to each other. All parts of the fluidic networks attached to both devices should also be matched, in order to create truly identical conditions in the two devices. This has not been achieved yet with the devices described in this thesis. Therefore, efforts toward improving the fluid delivery system must primarily focus on using available die space to create equivalent fluidic networks for both devices in a pair.

Other useful improvements in fluidics include reducing the "dead volume" in the PDMS, adding integrated valves in multi-level PDMS [27] for sample flow control, and ultimately, wafer-level fluidic integration.

With this in mind, work is in progress on integrated wafer-level anodic bonding to the device wafer of Pyrex (borosilicate glass) wafers with etched microchannels. This should allow much higher pressures for fluid delivery and much more robust packaging. It is anticipated that this will be fairly difficult to achieve, and will be a long-term goal for the next device generation.

APPENDIX A
FABRICATION DETAILS

Below we explain in some detail the two fabrication processes used throughout the work described in this thesis. Both processes use three masks, and either mask set can be used with either process to yield the same result. Some key issues for each process are discussed below, and the detailed fabrication steps are shown on the following pages.

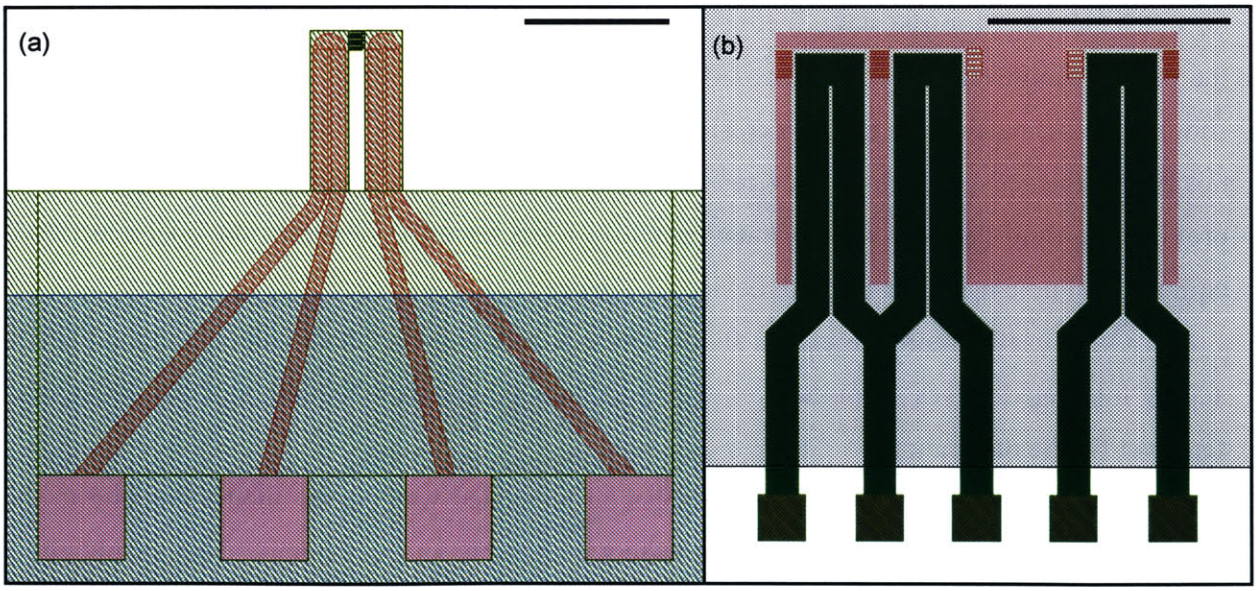

Figure A.1: Cantilever mask layouts. (this is the same as Figure 2.3, repeated here for easy reference) CAD mask layouts for (a) the bonded nitride process, and (b) the sacrificial polysilicon process. Black scale bar is 500 μm.

A.1 Bonded Nitride Process

Device fabrication begins by etching the channels (mask 1) into a silicon wafer with a reactive ion etcher (RIE). Next, low-stress silicon nitride is deposited on the wafer and a second, unpatterned wafer. The nitride surfaces of both wafers are smoothed using chemical mechanical polishing (CMP) and the polished nitride layers are then bonded together. The top nitride layer of the unpatterned wafer is dry-etched away, and all of the exposed silicon is removed with potassium hydroxide (KOH) to access the now-bonded double-layer devices. The cantilever outlines and channel port openings are etched into the nitride (mask 2) by RIE and the backside nitride is etched (mask 3) to create openings for the appropriate wafer through-holes. Finally, the silicon wafer is etched in KOH such that the cantilevers overhang from a silicon die.

In figure A.1(a), the channels etched in silicon with mask 1 are shown in red, green indicates the cantilever outline and the top edge of silicon die (mask 2), and blue is the backside nitride edge (mask 3) which produces the wafer through-hole outlined in white.

The critical steps for this process are the CMP and bonding of the nitride layers. These steps are based on the work of the Elwenspoek group at the University of Twente [28, 29]. They have achieved satisfactory bonding between nitride layers, after polishing the nitride to have surface roughness of less than 0.5 nm. However, it is unclear if the bond strength can be good enough to form a robust freestanding structure. Efforts at fabricating devices this way have so far shown bond yields of at most 60% after top wafer etch back, with most of the devices breaking and delaminating after further processing. Currently, the utility of this process remains questionable at best.

A.2 Sacrificial Polysilicon Process

This process starts identically, using mask 1 to RIE the channels in silicon. Next, low-stress silicon nitride is deposited on the wafer, followed by a polysilicon deposition that is slightly thicker than the depth of the initial etch. The polysilicon is CMP-ed down to the nitride surface, such that only polysilicon filling the trenches remains. At this point, a second low-stress SiN_x layer is deposited, as identical to the first as possible (for stress matching). Again, as in the

first process, the cantilever outlines and channel port openings are etched into the nitride (mask 2) by RIE and the backside nitride-poly-nitride multilayer is etched (mask 3) to create the back-side openings for KOH. The final KOH etch not only releases the cantilevers, but also etches out the sacrificial poly from inside the channels, creating the hollow structures.

In Figure A.1(b), the fluid channels of mask 1 are shown in green, the red shape is the topside cut in the silicon nitride that defines the cantilever shapes and the through-hole opening from the front, and gray is the backside mask outline which defines the KOH release from the back side (the white is unpatterned bulk silicon in this case, not open space).

In this process, the sacrificial channel etch-out is the critical step. The sacrificial poly etch rate is comparable to the bulk silicon rate of ~0.8 μm/min., despite the constricted dimensions of the cantilever channel. However, the etch must continue for ~17 hours to completely clear the cantilever channels, which is considerably longer than the ~7 hours that the through-wafer etch takes. This causes significant undercutting of the die and cantilevers (see light-colored rectangles around nitride opening in Fig. 2.8) – techniques are being explored to improve the anisotropy and selectivity of KOH to the different crystal planes of silicon in order to correct this. A more robust, but more complicated solution, is to separate the release and sacrificial etch-out steps, first opening only the channel ports to access the cantilever channels and etching out the poly in KOH, and only later etching wafer openings and releasing the cantilevers.

The following pages show the detailed fabrication process steps for the two processes described above, using the facilities at the MTL and in the Manalis Lab at the Center for Bits and Atoms within the MIT Media Laboratories.

A.3 Damascene CMP Sacrificial poly-Silicon Fabrication Process Steps

#	Step	Machine	Lab	parameters
1		HMDS	TRL	HMDS, prg. 5
	photoresist	coater	TRL	OCG825, 1um
		pre-bake	TRL	90C, 30min
	MASK 1	EV1	TRL	2.5s
	develop	photo-wet-l	TRL	OCG934 1:1
		post-bake	TRL	120C, 30min

2	etch Silicon	RIE (green)	ML*	1-2um
3	clean & strip resist	pre-metal piranha	ICL	blue beaker, 10min

4	rca clean	RCA	ICL	
	low-stress Nitride	VTR	ICL	0.5-1um

5	rca clean	RCA	ICL	
	LPCVD Polysilicon	6B-nPoly	ICL	2um

6	CMP Polysilicon	CMP	ICL	stop at nitride
	post-CMP clean	pre-metal piranha	ICL	10min blue + 10min green beaker

7	rca clean	RCA	ICL	
	low-stress Nitride	VTR	ICL	0.5-1um
8		HMDS	TRL	HMDS, prg. 5
	photoresist (2 sides)	coater	TRL	OCG825, 2x 1um
		pre-bake	TRL	90C, 30min
	MASK 2+3 (front+bck)	EV1	TRL	2.5s
	develop	photo-wet-l	TRL	OCG934 1:1
		post-bake	TRL	120C, 30min

9	etch Nitride + Poly	RIE (green)	ML*	front & backside
	ash resist	RIE (green)	ML*	

10	release etch	KOH (green)	ML*	80 C; ~0.8 um/min

silicon
Polysilicon
low-stress silicon nitride (SiN_x)

*ML = Manalis Lab

A.4 Direct-bonded Silicon Nitride Fabrication Process Steps

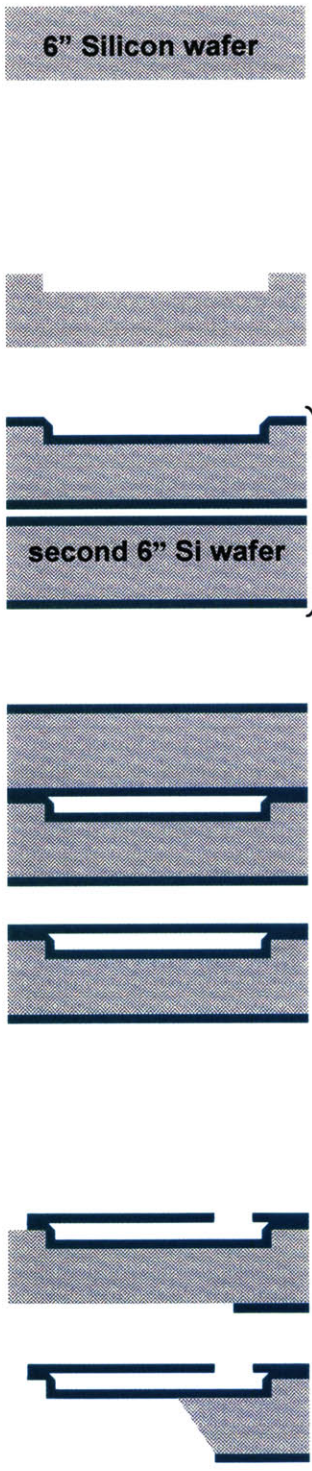

#	Step	Machine	Lab	parameters
1		HMDS	TRL	HMDS, prg. 5
	photoresist	coater	TRL	OCG825, 1um
		pre-bake	TRL	90C, 30min
	MASK 1	EV1	TRL	2.5s
	develop	photo-wet-l	TRL	OCG934 1:1
		post-bake	TRL	120C, 30min
2	etch Silicon	LAM490B	ICL	0.5-1 um
3	clean & strip resist	pre-metal piranha	ICL	blue beaker, 10min
	(add unpatterned clean 6" wafer before VTR deposition)			
4	low-stress Nitride	VTR	ICL	0.5-1 um (both wafers)
5	CMP nitride	CMP	ICL	< 0.5 nm roughness (both wafers)
	post-CMP clean	double piranha + 50:1 dilute HF	TRL	10min yellow + 10min green piranha + 10 min HF
7	rca clean	RCA	TRL	
	direct fusion bond	EV501	TRL	~ 1 mbar pressure 2000 N piston force
	anneal	tube B3	TRL	4 hrs @ 500 C
8	etch Nitride	RIE (green)	ML*	etch back top layer
	etch Silicon	KOH (green)	ML*	etch away top wafer
8		HMDS	TRL	HMDS, prg. 5
	photoresist (2 sides)	coater	TRL	OCG825, 2x 1um
		pre-bake	TRL	90C, 30min
	MASK 2+3 (front+bck)	EV1	TRL	2.5s
	develop	photo-wet-l	TRL	OCG934 1:1
		post-bake	TRL	120C, 30min
9	etch Nitride	AME5000	ICL	front & backside
	ash resist	asher	ICL	
10	release etch	KOH (green)	ML*	80 C; ~0.8 um/min

*ML = Manalis Lab

silicon
low-stress silicon nitride (SiN_x)

REFERENCES

[1] I. Wadsö. "Isothermal Microcalorimetry: Current problems and Prospects," *Journal of Thermal Analysis and Calorimetry* **64**, 75 (2001).

[2] I. Wadsö, "Trends in isothermal microcalorimetry," *Chemical Society Reviews* **26**, 79 (1997).

[3] Stephen E. Bialkowski *Photothermal Spectroscopy Methods for Chemical Analysis.* John Wiley & Sons, New York, 1996.

[4] E.A. Johannessen, J.M.R. Weaver, P.H. Cobbold, J.M. Cooper, "Heat conduction nano-calorimeter for pl-scale single cell measurements," *Applied Physics Letters* **80** (2002) 2029.

[5] R. Berger, Ch. Gerber, J.K. Gimzewski, E. Meyer, H.-J. Güntherodt, "Thermal analysis using a micromechanical calorimeter," *Applied Physics Letters* **69** (1996) 40.

[6] J.R. Barnes, R.J. Stephenson, C.N. Woodburn, S.J. O'Shea, M.E.Welland, T. Rayment, J.K. Gimzewski, Ch. Gerber, "A femtojoule calorimeter using micromechanical sensors," *Review of Scientific Instruments* **65** (1994) 3793.

[7] S.C. Minne, S.R. Manalis, C.F. Quate, "Parallel atomic force microscopy using cantilevers with integrated piezoresistive sensors and integrated piezoelectric actuators," *Applied Physics Letters* **67** (1995) 3918.

[8] S.R. Manalis, S.C. Minne, A. Atalar, C.F. Quate, "Interdigital cantilevers for atomic force microscopy," *Applied Physics Letters* **69** (1996) 3944.

[9] P. Vettiger, M. Despont, U. Drechsler, U. Durig, W. Haberle, M.I. Lutwyche, H.E. Rothuizen, R. Stutz, R. Widmer, G.K. Binnig, "The 'Millipede:' – more than one thousand tips for future AFM data storage," *IBM Journal of Research and Development* **44** (2000) 323.

[10] K Wilder, C.F. Quate, " Scanning probe lithography using a cantilever with integrated transistor for on-chip control of the exposing current," *Journal of Vacuum Science & Technology B* **17** (1999) 3256.

[11] J.K. Gimzewski, Ch. Gerber, E. Meyer, and R. R. Schlittler, "Observation of a chemical reaction using a micromechanical sensor," *Chemical Physics Letters* **217** (1994) 589.

[12] P.G. Datskos, M.J. Sepaniak, C.A. Tipple, N. Lavrik, "Photomechanical chemical microsensors," *Sensors and Actuators B* **76** (2001) 393.

[13] T. Thundat, G.Y. Chen, R.J. Warmack, D.P. Allison, E.A. Wachter, "Vapor Detection Using Resonating Microcantilevers," *Analytical Chemistry* **67**(1995) 519.

[14] M.K. Baller, H.P. Lang, J. Fritz, Ch. Gerber, J.K. Gimzewski, U. Drechsler, H. Rothuizen, M. Despont, P. Vettiger, F.M. Battiston, J.P. Ramseyer, P. Fornaro, E. Meyer, H.-J. Güntherodt, "A cantilever array-based artificial nose", *Ultramicroscopy* **82** (2000) 1.

[15] A.M. Moulin, R.J. Stephenson, M.E. Welland, "Micromechanical thermal sensors: Comparison of experimental results and simulations," *Journal of Vacuum Science & Technology B* **15** (1997) 590.

[16] C.A. Savran, A.W. Sparks, J. Sihler, J. Li, W. Wu, D. Berlin, J. Fritz, M.A. Schmidt, and S.R. Manalis "Fabrication and characterization of a micromechanical sensor for differential detection of nanoscale motions," *IEEE J. Microelectromechanical Systems* **11** (2002) 703.

[17] J. Fritz, M.K. Baller, H.P. Lang, H. Rothuizen, P. Vettiger, H.-J. Güntherodt, Ch. Gerber, J.K. Gimzewski, "Translating biomolecular recognition into nanomechanics," *Science* **288** (2000), 316.

[18] E.B. Cooper, J. Fritz, G. Wiegand, P. Wagner, S.R. Manalis, "Robust microfabricated field-effect sensor for monitoring molecular adsorption in liquids," *Applied Physics Letters* **79** (2001), 3875.

[19] T.P. Burg and S.R. Manalis, "Suspended microchannel resonators for biomolecular detection," to appear in *Applied Physics Letters* **83** (September 15, 2003).

[20] N.C. Loh, M.A. Schmidt, S.R. Manalis, "Sub-10 cm^3 interferometric accelerometer with nano-g resolution," *Journal of Microelectromechanical Systems,* **11** (2002), 182.

[21] C.A. Savran, T.P. Burg, J. Fritz and S.R. Manalis "Microfabricated mechanical biosensor with inherently differential readout," *Applied Physics Letters* **83** (2003) 1659.

[22] G.G. Yaralioglou, A. Atalar, S.R. Manalis, C.F. Quate, "Analysis and design of an interdigital cantilever as a displacement sensor," *Journal of Applied Physics* **83** (1998) 7405.

[23] D.C. Duffy, J.C. McDonald, O.J.A.Schueller, G.M. Whitesides, "Rapid Prototyping of Microfluidic Systems in Poly(dimethylsiloxane)," *Analytical Chemistry* **70** (1998) 4974.

[24] N.C. Loh, "High-resolution Micromachined Interferometric Accelerometer," M.S. Thesis, Massachusetts Institute of Technology, Cambridge, MA (2001).

[25] "PhotochemCAD: A computer-aided design and research tool in photochemistry," online resource at: http://omlc.ogi.edu/spectra/PhotochemCAD/html/du98.html.

[26] H. Du, R. A. Fuh, J. Li, A. Corkan, J. S. Lindsey, "PhotochemCAD: A computer-aided design and research tool in photochemistry," *Photochemistry and Photobiology,* **68** (1998) 141.

[27] T. Thorsen, S.J. Maerki, S.R. Quake, "Microfluidic large-scale integration," *Science* **298** (2002) 580.

[28] C. Gui, M. Elwenspoek, N. Tas, J.G.E. Gardeniers, "The effect of surface roughness on direct wafer bonding," *J. Applied Phyiscs* **85**, 7448 (1999).

[29] C. Gui, "Direct Wafer Bonding With Chemical Mechanical Polishing; Applications in Sensors and Acutators." PhD Dissertation, University of Twente, Enschede, Netherlands (1998).